Title
Discovering how inner nuclear membrane protein, LEM2, orchestrates timely nuclear envelope reformation during open mitosis

Author
Johnson, Isabel Emily

Publication Date
2020

Peer reviewed|Thesis/dissertation

Discovering how inner nuclear membrane protein, LEM2, orchestrates timely nuclear envelope reformation during open mitosis

by

Isabel Emily Johnson

DISSERTATION

Submitted in partial satisfaction of the requirements for degree of

DOCTOR OF PHILOSOPHY

in

Biochemistry and Molecular Biology

in the

GRADUATE DIVISION

of the

UNIVERSITY OF CALIFORNIA, SAN FRANCISCO

Approved:

DocuSigned by:
Adam Frost
1E2FF75D7B5A48F...

Adam Frost

Chair

DocuSigned by:
Peter Walter

Peter Walter

DocuSigned by:
David Toczyski
402B6252FD6D45E...

David Toczyski

Committee Members

Acknowledgments

First, I would like to thank the scientists who inspired me to pursue a biochemistry doctorate degree, David Pagliarini, Jonathan Stefely, and Andrew Reidenbach. As an undergraduate student, they took a chance on me and showed me that scientific research could be messy, exhilarating, and an incredibly fulfilling career.

Next, I would like to thank my thesis advisor, Adam Frost, for his mentorship and support over the last five years. Adam always made time for deep conversations about science and life. I'm grateful for the countless hours we spent at the whiteboard, brainstorming and challenging each other as peers. From him I learned the satisfaction that comes from working on incredibly difficult questions, and to fearlessly follow my scientific curiosity wherever it might take me. I'll take these lessons with me wherever I go.

UCSF has been a rich environment to learn in, filled with inspiring scientists who are always willing to share their time and expertise. I'm thankful to my rotation mentor, Martin Kampmann, for teaching me to write an effective research proposal. I also thank my thesis committee members, Peter Walter and Dave Toczyski, for giving me the space to reason through my science, and for pushing me to deeply evaluate what makes me happy in lab and in life.

The Frost lab has been family to me through these past five years. Together we have celebrated in times of success, wallowed in times of hardship, and always taken the time for a beer (or a few) when necessary. I couldn't have done this without them, and I'm forever grateful for their support. Specifically, I'd like to thank Raghav Kalia for his wisdom and friendship, and Lillian Kenner and Lakshmi Miller-Vedam, for rooting for me and showing me the way. I am especially grateful to Alexander von Appen, who invited me to collaborate with him at one of my lowest points in grad school. We spent years doing science side by side and achieved an amazing scientific partnership and friendship that I'll always be grateful for.

I'd like to thank my parents, Carmen and Darren, and my sister, Josie, for showing me that what is important in life is hard work, integrity, kindness, and humor. They have been my anchor, deeply empathizing with me through every win and every loss. I'm eternally thankful for them.

I'd also like to thank Janine, Peter, and Brian Bassano. They welcomed me into their family and provided me with warm encouragement and support from day one. I am grateful to know them and to be part of their family.

I have been lucky to have an incredible community of friends and in San Francisco. Our camping trips and family dinners got me through. I'd especially like to thank Ben Blumenfled, Elena Thomas, Paul Kiernan, Taylor Oniskey, Leah Lurye, and Ruby Valadez for their friendship.

Most of all, I'd like to thank my love, Chris Bassano. Chris uprooted his life to move with me to San Francisco. Over the past five years, he has nurtured me, celebrated with me, and believed in me even when I couldn't believe in myself. I would not be here without his love and support through it all.

Contributions

von Appen, A.[†], LaJoie, D. [†], Johnson, I. E. [†], Trnka, M. J., Pick, S. M., Burlingame, A. L., Ullman, K. S., Frost, A. 2020. A role for liquid-liquid phase separation in ESCRT-mediated nuclear envelope reformation. *bioRxiv.* 577460. doi:10.1101/577460.

Discovering how inner nuclear membrane protein, LEM2, orchestrates timely nuclear envelope reformation during open mitosis

By

Isabel Emily Johnson

Abstract

Membranes are fundamental to cellular life. They define the cellular border and establish biochemically specialized subcellular compartments. As cell grow, change, and divide, cellular membranes are remodeled accordingly: undergoing membrane fission and fusion to maintain cellular architecture. For example, the nuclear membrane that organizes and protects DNA is remodeled during cell division[2]. In cells that undergo "open mitosis", the nuclear membrane is fully disassembled to allow chromosomes to be segregated by the spindle apparatus and reassembled following chromosome segregation[10]. Understanding how cells remodel nuclear membranes to rebuild nuclei with every cell division is critical to understanding the core principals of membrane biology that underlie cellular life.

In my dissertation, I describe how a membrane fusion complex is organized to seal holes in the reforming nuclear envelope that are occupied by spindle microtubules. Using biochemical approaches, I find that an inner nuclear membrane protein, called LEM2, uses multivalent, low-affinity binding interactions to condense in a liquid-like phase at the junction of the nuclear envelope, chromatin, and residual spindle microtubules. There, LEM2 activates the ESCRT protein, CHMP7, in a looping copolymer. Together, the fluid LEM2 toroid and structured LEM2-CHMP7 copolymer collaborate to serve as a molecular "O-ring" for early nuclear sealing. Furthermore, the LEM2-CHMP7 ring serves as a foundation for the membrane-remodeling ESCRT-III complex to execute coupled spindle disassembly and membrane fusion. This work establishes a new paradigm in membrane organization, in which a liquid-like protein phase can function as both a barrier within a discontinuous membrane and a scaffold for membrane fusion factors.

Table of Contents

List of Figures

List of Tables

Phase separation by the membrane protein LEM2 governs ESCRT-mediated nuclear envelope reformation

Contributing authors

Alexander von Appen[1†], Dollie LaJoie[2†], Isabel E. Johnson[1†], Michael J. Trnka[3], Sarah M. Pick[4], Alma L. Burlingame[3], Katharine S. Ullman[2]*, Adam Frost[1,5,6]*

[1]Department of Biochemistry and Biophysics, University of California, San Francisco, San Francisco, CA, USA

[2]Department of Oncological Sciences, Huntsman Cancer Institute, University of Utah, Salt Lake City, UT, USA

[3]Department of Pharmaceutical Chemistry, University of California, San Francisco, San Francisco, CA, USA

[4]Faculty of Chemistry and Pharmacy, University of Freiburg, Freiburg, Germany

[5]Chan Zuckerberg Biohub, San Francisco, CA, USA

[6]Quantitative Biosciences Institute, University of California, San Francisco, CA, USA

†A.v.A., D.L., and I.E.J. contributed equally to this work

*Co-corresponding authors: katharine.ullman@hci.utah.edu, and adam.frost@ucsf.edu.

Preface

The bulk of this thesis appears as von Appen, A., LaJoie, D., and Johnson, I.E. et al. preprinted in *bioRxiv* in 2019, and accepted for publication in *Nature* in 2020.

The results presented in this thesis follow from work published by Mingyu Gu, Dollie LaJoie, and Opal S. Chen[17], and are the product of a strong collaboration with co-authors Alexander von Appen and Dollie LaJoie of the Frost and Ullman labs. Specifically, I designed, performed, and analyzed turbidimetry and analytical size exclusion experiments. I designed, performed, and analyzed in vitro fluorescent and negative stain electron microscopy experiments, both independently and collaboratively with Alexander von Appen. All cellular imaging experiments, except for STED, were performed and analyzed by Dollie LaJoie; STED imaging was performed and analyzed by Alexander von Appen. The crosslinking-mass spectrometry, CHMP7 pelleting, and CHMP7 structural studies were performed and analyzed by Alexander von Appen with support from Michael J. Trnka and Sarah M. Pick. Adam Frost and Katharine S. Ullman supervised the work.

Endosomal Sorting Complexes Required for Transport-III (ESCRT-III) proteins polymerize into membrane remodeling filaments with the help of the AAA+ ATPase, Vps4[21,23]. Since their discovery at endosomal membranes for the formation of multivesicular bodies, ESCRT-III proteins have been implicated at nearly every membrane within the cell[28]. It remains unclear how ESCRT-III proteins are assembled at diverse sites of action with spatiotemporal precision, how ESCRT-III proteins are so adaptable to vast membrane dimensions, and how conformational changes in individual ESCRT-III subunits propagate to large-scale changes in membrane architecture to achieve complete membrane fission and fusion. To uncover ESCRT-III roles in the fission yeast, *Schizosaccharomyces pombe*, Gu, M. et al., sought to learn how cells might be affected by the loss of Vps4. What they found was that Δvps4 *S. pombe* grew very slowly and had nuclear envelope defects. Serendipitously, Gu et al. found that these mutant phenotypes could be rescued by suppressor mutations in two proteins: Cmp7p or Lem2p. Evaluating the roles of homologous human proteins in a mammalian system, the authors found that the inner nuclear membrane protein, LEM2, recruited the ESCRT-II/III chimera protein, CHMP7, to the

reforming nuclear envelope during anaphase, and that CHMP7 recruitment to the reforming nuclear envelope was required for downstream ESCRT-III recruitment. Further, they found that the C-terminal winged helix domain of LEM2 could bind directly to CHMP7 in vitro, consistent with a role for LEM2 as a site-specific ESCRT adaptor at the nuclear envelope[17].

This laid the foundation for our mechanistic study, in which we aimed to dissect how the two-pass inner nuclear membrane protein, LEM2, serves as a site-specific ESCRT adaptor at the nuclear envelope through the unusual chimera ESCRT-II/ESCRT-III protein, CHMP7.

Abstract

Spindle disassembly and nuclear envelope (NE) reformation during late anaphase require the Endosomal Sorting Complexes Required for Transport (ESCRTs) and the inner nuclear membrane protein, LEM2. Here, we show how LEM2's ability to undergo liquid-like phase separation around spindle microtubules governs these processes. The LEM-domain of LEM2 binds to the chromatin-coating protein barrier-to-autointegration factor (BAF), where LEM2's low complexity domain (LCD) condenses into a liquid-like phase. A proline-arginine-rich sequence within LEM2's low complexity domain (LCD), adjacent to the first transmembrane helix, binds microtubules and this targets LEM2 condensation to gaps in the nascent NE occupied by spindle microtubules. There, LEM2's winged-helix (WH) domain activates and, unexpectedly, co-polymerizes with the ESCRT-II/ESCRT-III hybrid protein, CHMP7, through a domain replacement mechanism. Disrupting these interactions precludes the recruitment of downstream ESCRT activities, prevents early nucleocytoplasmic compartmentalization, and leads to defects in spindle disassembly and genome integrity. LEM2's LCD, moreover, is mitotically phosphorylated, and phosphomimetic mutations abrogate its ability to phase separate. Thus, we propose that upon dephosphorylation at mitotic exit, LEM2 condenses and collaborates with CHMP7 to form a molecular "O-ring" at the confluence between nuclear membranes, chromatin, and residual spindle microtubules to promote reformation of the nucleus.

Introduction

At the onset of "open" mitosis in mammalian cells, the nuclear envelope (NE) dissociates from the chromatin surface to allow for chromosome singularization and segregation by the mitotic spindle[1,2]. Mitotic phosphorylation events disrupt the affinity of inner nuclear membrane (INM) proteins for the chromatin surface, enabling the NE to recede into the contiguous endoplasmic reticulum[2]. During anaphase, a program of phosphatases reverses this process, and INM proteins within the endoplasmic reticulum membrane regain affinity for DNA or DNA-binding partners to coat each mass of condensed chromosomes, referred to as the chromatin disk, with nascent nuclear membranes[3–6].

During nuclear envelope reformation, barrier-to-autointegration factor (BAF) cross-bridges anaphase DNA to restrict membrane access to the surface of the disk and ensure the formation of a single nucleus[7]. As the nascent NE surrounds the chromatin disk, a subset of the nuclear membrane proteome transiently segregates into a distinct core region that coincides with microtubules (MTs) emanating from centrosomes on the outer face of the disk and with central spindle MTs on the inner face of the disk[8–11]. The molecular determinants that drive proteins to either the core or non-core regions remain unknown, although a role for spindle MTs themselves has been proposed[11,12]. Of the INM proteins that enrich in the core, several belong to the LEM (Lap2-Emerin-MAN1) domain family of proteins. These proteins are characterized by low complexity domains (LCDs), interactions with the nuclear lamina, and, for Lap2 and Emerin, their ability to bind to BAF via a conserved LEM-domain, the hallmark motif that defines this family[13]. Recent studies reported that another conserved INM LEM-domain containing protein, LEM2[14–16], is a nucleus-specific adaptor for the ESCRT machinery[17–19]. The ESCRT machinery then recruits factors involved in spindle disassembly and catalyzes a poorly understood membrane remodeling reaction that seals the nuclear envelope[9,17–24]. Deploying this pathway with spatiotemporal precision is critical because errors lead to genome instability and nuclear malformations[9,12,17,20,24–26]. Yet, it remains unclear how LEM2 triggers ESCRT activities specifically around the microtubule-containing fenestrations that persist in the reforming NE during the critical ~8-minutes when the NE reforms[8].

The membrane-associated protein, CHMP7, is the most upstream ESCRT-III domain-containing protein at the reforming NE[9,17,20,27]. CHMP7 is also unique amongst the twelve human ESCRT-III proteins because its canonical ESCRT-III domain is preceded by an N-terminal tandem winged-helix (WH) domain[28]. This domain is homologous to VPS25, a member of the ESCRT-II complex, which can nucleate ESCRT-III filament formation in other contexts[29,30]. Whether CHMP7 nucleates polymerization of other ESCRT-III proteins via its VPS25-like domain, or whether it can polymerize itself remains unknown. More broadly, the molecular mechanisms that govern ESCRT-III activities specifically at the interface of decondensing chromatin, the mitotic spindle, and the reforming nuclear envelope for coordinated membrane fusion and spindle disassembly remain unclear.

Protein phase separation, or the formation of biomolecular condensates, is now an established mechanism for organizing dynamic cellular processes through the creation of membraneless but biochemically-specialized compartments[31–33]. Here we show that LEM2 undergoes liquid-like phase separation at the membrane-microtubule-chromatin interface to rapidly concentrate around the residual spindle MTs that obstruct nuclear membrane fusion. There, LEM2 activates CHMP7 polymerization via a domain-replacement copolymerization mechanism, and this leads to downstream ESCRT-III and cofactor recruitment. This process ultimately seals the reforming nucleus by initiating spindle clearance and fusion of the nuclear envelope.

Results

LEM2 clustering in the core region of the NE depends on a liquid droplet-forming domain.

In late anaphase, as the nascent NE surrounds the chromatin disk, we observed LEM2 concentrate progressively along the NE core. This core-concentrating behavior was in contrast to the localization pattern of the non-core marker, Lamin B2, and to LEM2's uniform distribution around the INM during interphase (**Fig. 1A**)[15,34]. To determine how LEM2 concentrates in the core region, we used live-cell imaging to monitor an allelic series of domain deletion LEM2-mChr constructs, alongside GFP-tubulin. Since, as expected, we found that LEM2's LEM domain bound with high affinity to BAF in vitro

(**Extended Data Fig. 1A-C**), we tested a LEM2 construct bearing a four amino acid (AA) substitution in the LEM domain ($LEM2_{m21}$) analogous to the m24 mutation that disrupts Emerin's ability to bind BAF[35]. This mutation was sufficient to disrupt LEM2 accumulation within the NE and subsequent core enrichment in anaphase cells. This phenotype is consistent with previous results showing that BAF itself is an early constituent of the core region[36] (**Fig. 1B, Extended Data Fig. 1A, B**). Unexpectedly, removing the adjacent LCD (DAA 43-202; $LEM2_{\Delta LCD}$) also compromised LEM2 nuclear envelope enrichment—despite the presence of an intact LEM motif—suggesting that the LEM domain and LCD are each necessary but neither is sufficient for targeting (**Fig. 1B**). By contrast, a large deletion within LEM2's C-terminal WH domain ($LEM2_{\Delta WH}$; DAA 415-485) did not affect LEM2 core localization (**Fig. 1B**).

To characterize the properties and role of LEM2's LCD in core localization, we purified LEM2's N-terminal nucleoplasmic domain (NTD), containing the LEM and LCD domains (AA 1-208; $LEM2_{NTD}$). The LCD is notable for its highly basic sequence bias (isoelectric point of 11.8) due to overrepresented Arginine (R), in addition to overrepresented Proline (P) and Alanine (A), residues (**Extended Data Fig. 1D**). After purification using high ionic-strength solutions, we observed that $LEM2_{NTD}$ spontaneously formed spherical droplets with liquid-like properties after exchange into physiological salt and pH. These $LEM2_{NTD}$ droplets could undergo complete droplet fusion and inter- and intra-droplet diffusion on the timescale of seconds **(Fig. 1C-E**). Complex coacervation with polyanions like DNA and RNA also promoted monodisperse $LEM2_{NTD}$ to condense into spherical liquid-like droplets—a property shared in common with other PR-rich proteins[37] (**Extended Data 2A**). Thus, LEM2's LCD promotes anaphase core condensation in cells and exhibits both liquid-like phase separation and complex coacervation properties in vitro.

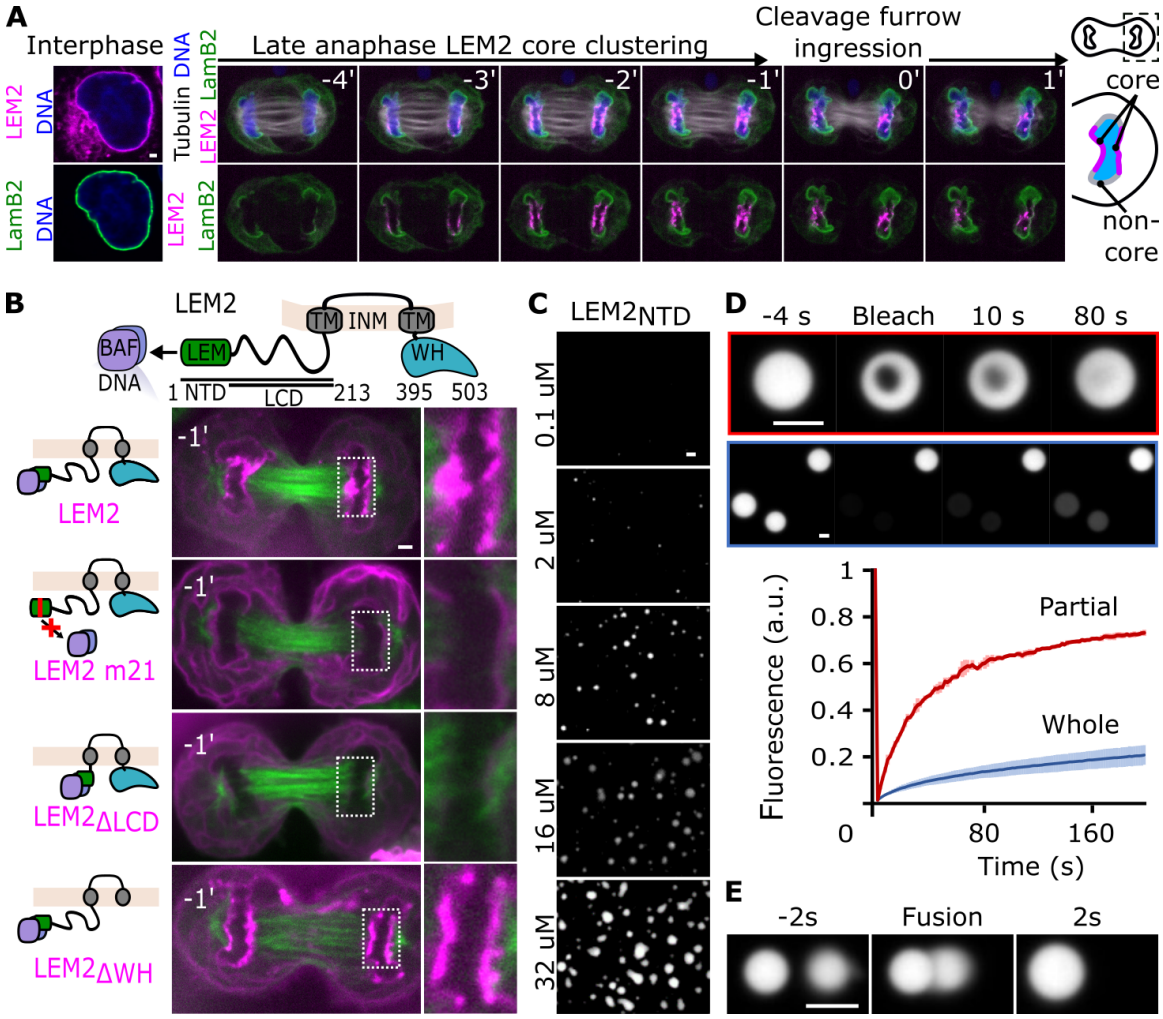

Fig. 1. LEM2 targeting to the core of anaphase chromatin disks depends on interaction with BAF and a region capable of forming liquid-like droplets.

(A) Live-cell imaging of GFP-Lamin B2 and LEM2-mChr; DNA is stained with NucBlue and tubulin visualized with SiR-tubulin. Time 0 refers to complete cleavage furrow ingression. (B) Top: Domain architecture of LEM2; TM – transmembrane. Bottom: Live cell imaging of GFP-tubulin alongside full or mutant LEM2-mChr. m21 mutation denotes alanine substitutions at AA 21-24. Time 0 refers to time of cleavage furrow ingression. (C) Concentration-dependent droplet formation of purified $LEM2_{NTD}$. (D) Partial and whole droplet fluorescence recovery after photobleaching (FRAP). N=3, bars are standard deviations (SD). (E) Real-time fluorescence imaging of $LEM2_{NTD}$-droplet fusion. Scale 2 um A-E.

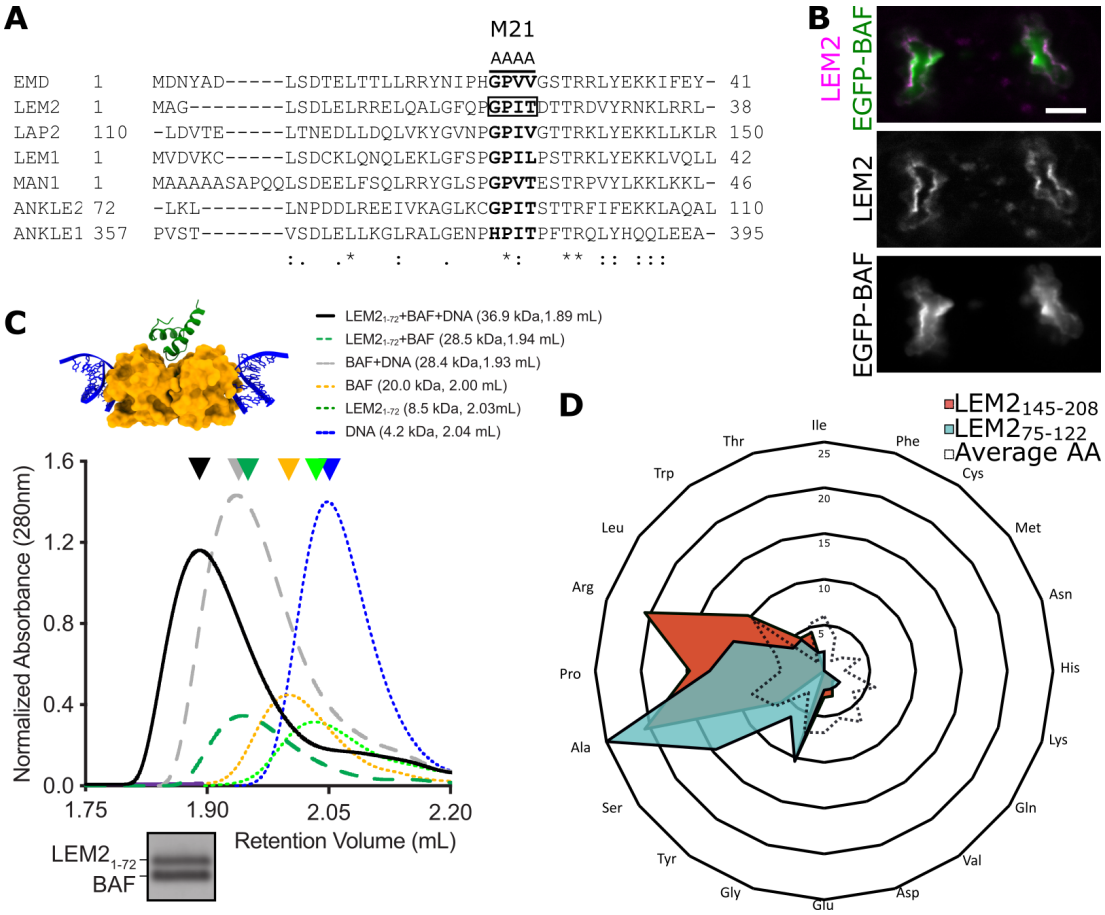

Extended Data Fig. 1. The N-terminus of LEM2 is characterized by a canonical BAF-binding LEM domain and a low complexity domain.

(A) Sequence alignment of LEM domains across LEM family proteins showing conservation of a four-amino acid (AA) sequence that, when mutated in EMD (EMDm24), disrupts BAF binding Position of analogous mutation in LEM2 ($LEM2_{m21}$) is indicated[35]. (B) HeLa cells stably expressing LEM2-mCherry and EGFP-BAF were live-imaged in anaphase. Scale 10 um. (C) Top: A homology model for $LEM2_{1-72}$ - BAF-DNA complex, based on high-resolution interfaces of BAF with DNA (2BZF), and BAF with LEM-domain of EMERIN (2ODG)[62,63]. Middle: Absorbance at 280 nm as a function of retention volume (mL) from analytical size exclusion chromatography. Retention volumes for major peaks (arrowheads) and predicted molecular weights for protein or protein-DNA complexes are listed. Bottom: SDS-PAGE of major peak for $LEM2_{1-72}$+BAF+DNA sample. (D) LEM2 low complexity domain amino acid composition compared to the average protein composition.

LEM2 can form a liquid-like coat on microtubule bundles.

Super-resolution STED microscopy of immunostained HeLa cells revealed that endogenous LEM2 enriched specifically in toroid-like shapes around spindle MTs at the chromatin surface (**Fig. 2A**). To probe if LEM2 can bind MTs directly, we tested binding in vitro with fluorescently labeled proteins. We observed by fluorescence microscopy that detergent-solubilized, purified full-length LEM2 ($LEM2_{FL}$) bound and stabilized MTs, and promoted MT bundling in vitro, at physiological salt and pH conditions that otherwise favor depolymerization of MTs (**Fig. 2B**). After reconstitution into proteoliposomes, moreover, membrane-embedded $LEM2_{FL}$ retained MT stabilizing and bundling activities (**Extended Data Fig. 2B**). Finally, we found that the isolated $LEM2_{NTD}$ was sufficient to bundle MTs, suggesting that LEM2's MT-bundling activity does not require the membrane-spanning region or the C-terminal WH domain **(Fig. 2C**).

To quantitatively map the LEM2 sequences that are required for MT binding, we used a light-scattering assay for MT-bundle formation, corroborated visually by negative stain electron microscopy (EM). Truncated protein constructs constituting other domains, such as the winged-helix domain (AA 395-503; $LEM2_{WH}$) and the distal N-terminal portion of LEM2 ($LEM2_{1-72}$), did not promote the formation of light-scattering MT bundles in vitro (**Extended Data Fig 2C**). However, $LEM2_{NTD}$, containing the LCD, bundled MTs in a concentration-dependent and saturable manner, with a half-maximal scattering concentration, or a $K_{apparent}$ value, of 1.3 μM (**Extended Data Fig. 2C**). Both $LEM2_{FL}$ and $LEM2_{NTD}$ bound MT bundles dynamically, recovering fluorescence at similar rates after photobleaching, in contrast to tubulin in the polymeric microtubule lattice, which did not recover (**Fig. 2D**). These data demonstrate that LEM2 binds MTs directly through its LCD and this causes MT-bundling in vitro.

Considering the liquid-like phase separation and complex coacervation properties of LEM2's LCD, we explored the physical state of MT-bound LEM2 in vitro. Using video fluorescence microscopy, we observed $LEM2_{NTD}$ droplets fuse with MT-bound $LEM2_{NTD}$ with dynamics suggestive of a continuous, liquid-like coating of LEM2 on the MT surface (**Fig. 2E**). Consistent with this notion, photobleached regions of $LEM2_{NTD}$ on MT bundles recovered fluorescence in flowing, liquid-like

gradients, rather than in a uniform recovery pattern across the bleached area (**Fig. 2E, Extended Data Fig. 2D**).

Furthermore, $LEM2_{NTD}$ droplets could concentrate unpolymerized tubulin by coacervation and form MT-bundles upon addition of GTP and $MgCl_2$ (**Extended Data Fig. 2A, E**). Negative stain EM revealed that LEM2-bundled MTs lost their characteristic tubulin lattice fine structure, apparently occluded by an amorphous LEM2 coating (**Fig. 2F**). Thus, LEM2 coats MTs in a liquid-like phase formed by its LCD.

To parse which molecular features of the LCD contribute to microtubule binding and phase separation, we used synthetic peptides tiled across the LCD sequence for in vitro assays. We identified two peptides within a P-R-rich region that were sufficient to induce MT bundling in vitro (**Fig. 2F, Extended Data Fig. 3A-E**). In vivo, a LEM2 mutant lacking this P-R-rich domain (DAA 145-213; $LEM2_{\Delta P\text{-}R}$) initially targeted to the nascent NE but did not enrich along the MT-containing core (**Fig. 2G, Extended Data Fig. 3F**). This behavior suggests that LEM2 requires its ability to bind MTs to target accurately during anaphase. Additionally, we found that another synthetic LEM2 LCD peptide with an S-Y-rich sequence[38] (AA 75 – 122; $LEM2_{S\text{-}Y}$) underwent robust liquid-like phase separation, even in the absence of polyanions in vitro (**Extended Data Fig. 3E**). This observation indicates that, like other S-Y rich peptides[38], LEM2's S-Y-rich region can mediate the multivalent, low-affinity interactions necessary for liquid-like phase separation. In vivo, a LEM2 mutant lacking the S-Y-rich region (DAA 75-123; $LEM2_{\Delta S\text{-}Y}$) localized properly to the core region of the nascent NE during anaphase, suggesting that MT binding is a primary determinant of anaphase core concentration (**Fig. 2G, Extended Data Fig. 3F**). In summary, we found that within the LCD of LEM2, a P-R-rich region mediates direct MT binding and is required for localization to spindle MTs during NE reformation, while an adjacent S-Y-rich region is sufficient for liquid-like phase separation.

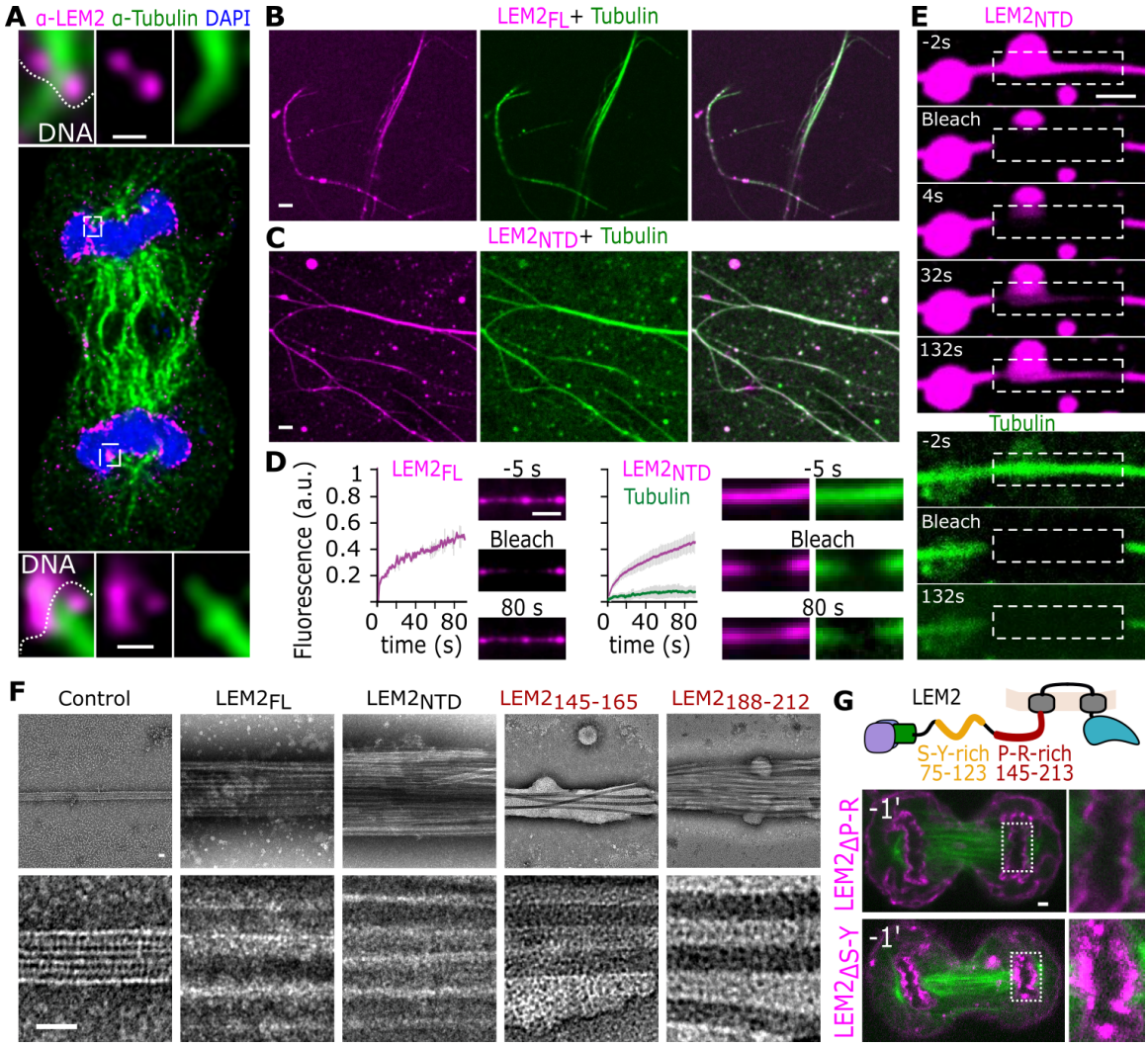

Fig. 2. LEM2 forms a liquid-like coating on microtubule bundles via microtubule binding domain within LCD.

(A) STED imaging of endogenous LEM2 in late anaphase. Scale 150 nm. (B) Purified full length LEM2 ($LEM2_{FL}$) mixed with MTs. (C) Purified $LEM2_{NTD}$ droplets mixed with MTs. (D) FRAP of $LEM2_{FL}$- and $LEM2_{NTD}$-coated MT bundles. (E) FRAP of $LEM2_{NTD}$-coated MT bundle. (F) Negative stain electron micrographs of MT alone or with indicated LEM2 constructs. Scale 25 nm. (G) Top: Domain architecture of LEM2. Bottom: Live cell imaging of indicated LEM2-mChr deletion constructs and GFP-tubulin. Time 0 refers to time of cleavage furrow ingression. Scale 2 um B-E, G.

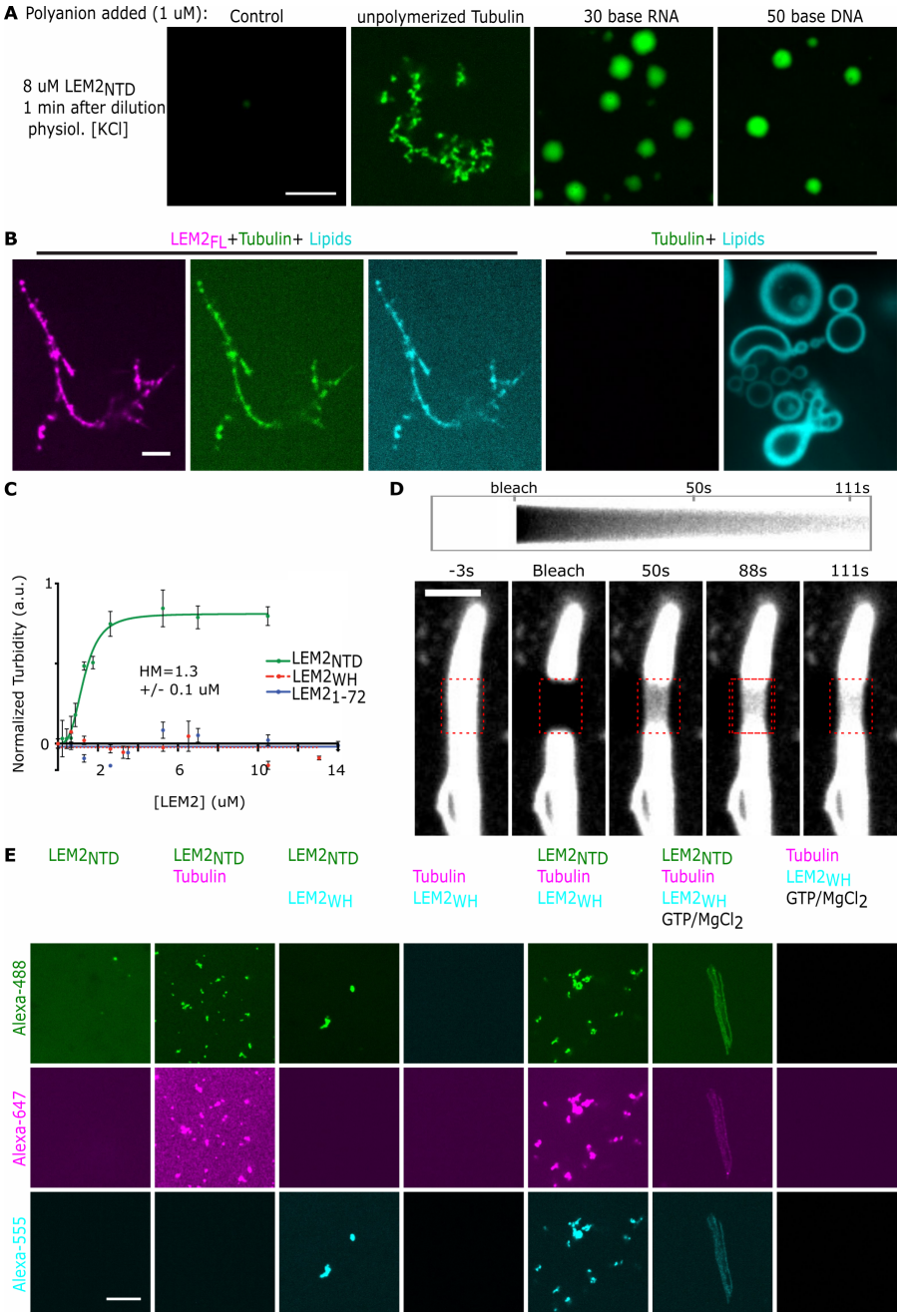

Extended Data Fig. 2. LEM2 forms coacervates with microtubules in a liquid-like coat.

(A) Fluorescence microscopy of purified $LEM2_{NTD}$ with indicated molecular anions. Scale 2 um. (B) Fluorescence imaging of indicated combinations of $LEM2_{FL}$-Alexa488 (magenta), Tubulin-Alexa647 (green), and lipids labeled with PE-rhodamine (cyan). Scale 2 um. Before imaging, the reactions were diluted from high ionic strength and detergent concentration to physiological ionic strength and detergent levels near the critical micelle concentration. (C) Light scattering-based quantification at 340 nm (turbidity) of MT bundling by indicated LEM2 constructs. Half maximal concentration of $LEM2_{NTD}$ is 1.303 uM +/- 0.1 uM. (D) Top: Kymograph of across bleached region. Bottom: FRAP of $LEM2_{NTD}$-coated MT bundle. Scale 2 µm. (E) Fluorescence microscopy of $LEM2_{NTD}$ Alexa488 in combination with Tubulin-Alexa647, $LEM2_{WH}$-Alexa555, and $GTP/MgCl_2$, as indicated. Scale 10 um.

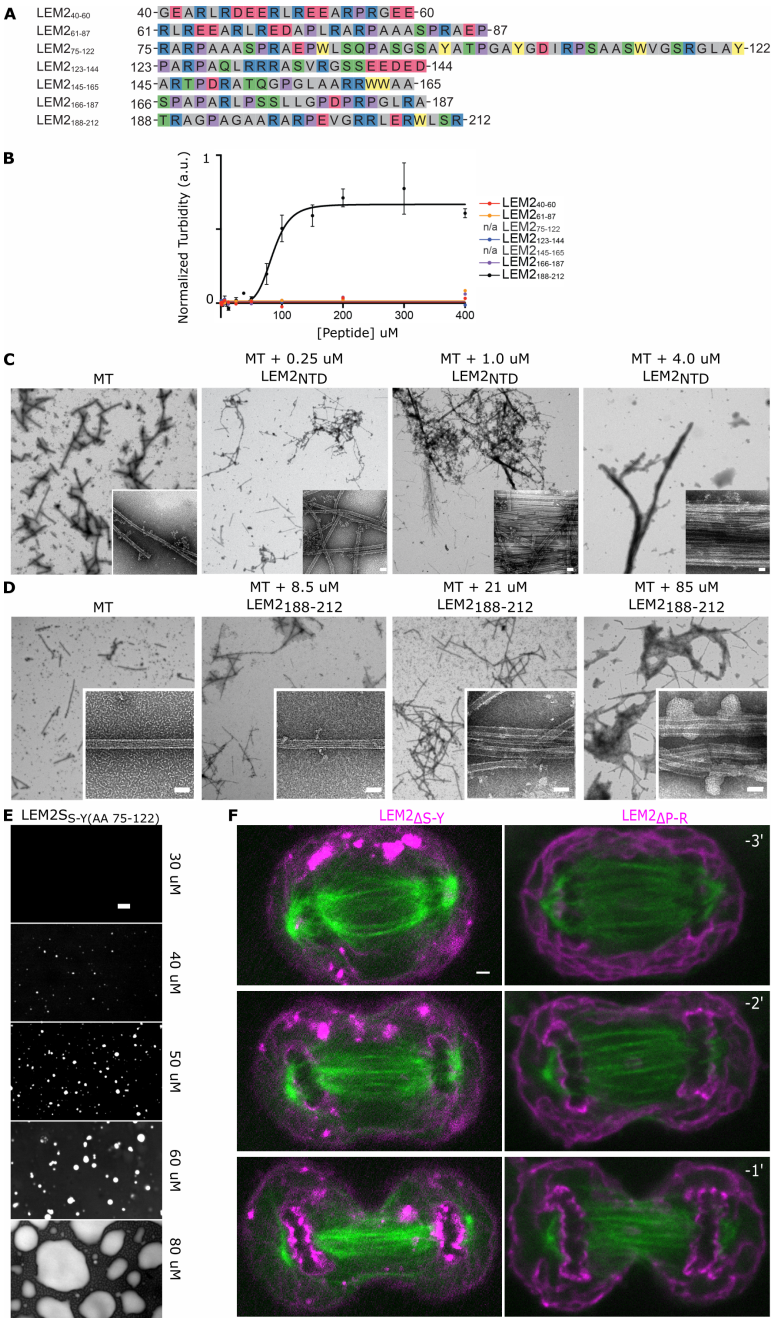

Extended Data Fig. 3. LEM2-LCD bundles microtubules in vitro through discrete MT-binding domain.

(A) Amino acid sequences of 7 consecutive LEM2 peptides tiling the LCD. (B) Light scattering-based quantification at 340 nm (turbidity) of MT bundling by indicated LEM2 peptides. Half maximal concentration of $LEM2_{188-212}$ is 85.11 uM. (C) Negative stain EM of MTs or MTs with indicated concentrations of $LEM2_{NTD}$, corresponding to turbidity reactions. Scale 25 nm. (D) Negative stain EM of MTs or MTs with indicated concentrations of $LEM2_{188-212}$, corresponding to turbidity reactions. Scale 25 nm. (E) Concentration-dependent droplet formation of $LEM2_{S\text{-}Y\text{-}rich}$ peptide. (F) Live cell imaging of indicated LEM2-mChr deletion constructs and GFP-tubulin. Time 0 refers to time of cleavage furrow ingression. Scale 2 um.

CHMP7 polymerization and LEM2 condensation promote early nuclear compartmentalization.

To investigate the functional roles of LEM2 condensation at the spindle-chromatin interface, we assessed how the timing of LEM2 core localization correlated with successful nuclear compartmentalization as NLS cargo transport resumes in anaphase. To do this, we measured nuclear accumulation of NLS-3GFP, a nuclear localization signal fused to three GFPs. Cells expressing siRNA-resistant full-length LEM2-mChr or $LEM2_{\Delta S\text{-}Y}$-mChr—under both control and endogenous LEM2-depletion conditions—accumulated NLS-3GFP in newly-formed nuclei. Notably, NLS-3GFP began concentrating within nuclei shortly following LEM2 core localization when spindle MTs still present a barrier to sealing the nascent NE (**Fig. 1A, Fig. 3A, Extended Data Fig. 4A,B**). In contrast, expression of $LEM2_{\Delta P\text{-}R}$-mChr, which encodes a protein that failed to concentrate within the core (**Fig. 2G**), significantly impaired timely NLS-3GFP accumulation (**Fig. 3A, Extended Data Fig. 4A**).

Additionally, expression of $LEM2_{\Delta WH}$-mChr, which localized to the core, also impaired timely NLS-3GFP accumulation, demonstrating that the WH domain plays a functional role in compartmentalization that is independent of LEM2 condensation (**Fig. 3A, Extended Data Fig. 4A**). We previously reported that LEM2's WH domain, also referred to as the MSC domain[39], directly binds to CHMP7 in vitro[17]. This observation suggested that delayed nuclear compartmentalization with expression of $LEM2_{\Delta WH}$ may be due to a failure to recruit CHMP7 and subsequent ESCRT pathway proteins. Accordingly, depletion of either LEM2 or CHMP7 impaired nuclear compartmentalization for an extended period, with defects persisting at least up to 30 minutes after complete cleavage furrow ingression (**Extended Data Fig. 4C**).

As expected by their direct binding relationship, the expression of $LEM2_{\Delta WH}$-mChr was unable to recruit GFP-CHMP7 to the NE (**Fig. 3B**). Furthermore, following depletion of endogenous LEM2, overexpression of siRNA-resistant $LEM2_{\Delta WH}$-mChr failed to rescue the recruitment of IST1, an ESCRT-III protein known to be downstream of LEM2 and CHMP7 and to be required for SPASTIN recruitment (**Fig. 3C, Extended Data Fig. 4D-E**)[9,17]. Overexpression of siRNA-resistant full-length LEM2 notably enhanced recruitment of endogenous IST1 to the nascent NE, as measured by premature recruitment to

chromatin disks (**Extended Data Fig. 4D-E, Table 1**). This early recruitment indicates that LEM2 guides both the spatial and temporal patterns of ESCRT activation.

To explain how LEM2 engages CHMP7 for early nuclear compartmentalization and ESCRT-III recruitment, we turned to in vitro reconstitution with purified proteins. Full-length, human CHMP7 purified as a stable monomer, and incubation of CHMP7 with $LEM2_{NTD}$ had no discernable effect on CHMP7's oligomeric state (**Fig. 3D left**). Incubation of CHMP7 with the C-terminal WH domain of LEM2 (AA 395-503; $LEM2_{WH}$), by contrast, triggered the assembly of multi-layered, looping protein polymers with a variable inner diameter that ranged from ~ 50 to 100 nm (**Fig. 3D right**). Model membranes were also sufficient to trigger polymerization of full-length CHMP7, with many polymers bound to the surface of the phospholipids (**Extended Data Fig. 4F**). 2D alignment and image averaging of these membrane-induced polymers, which were in a favorable orientation for subsequent classification, revealed a repeating unit comprised of a continuous, polymeric strand studded with repeating perpendicular spikes (**Fig. 3E, Extended Data Fig. 4G**).

The dimensions of the periodic features in this polymer match those of the homologous structure of "open" conformation human CHMP1B polymers and yeast Snf7 polymers, suggesting these structures comprise an ESCRT-III domain polymeric strand decorated with protruding ESCRT-II-like tandem WH-domains[30,40,41] (**Fig. 3E, Extended Data Fig. 4G, Table 2**). Consistent with this model, a truncated CHMP7 fragment comprised only of the ESCRT-III domain (AA 229-453; $CHMP7_{ESCRT-III}$) spontaneously polymerized during purification into rings devoid of perpendicular spikes, but with a comparable diameter to full-length CHMP7 (**Fig. 3F**). The spontaneous polymerization of $CHMP7_{ESCRT-III}$ further suggests a potential auto-inhibitory function for CHMP7's N-terminal WH domains. In summary, we found that LEM2's WH activates an apparently autoinhibited CHMP7 monomer for polymerization, and these functions mediate early nuclear compartmentalization and downstream ESCRT-III recruitment.

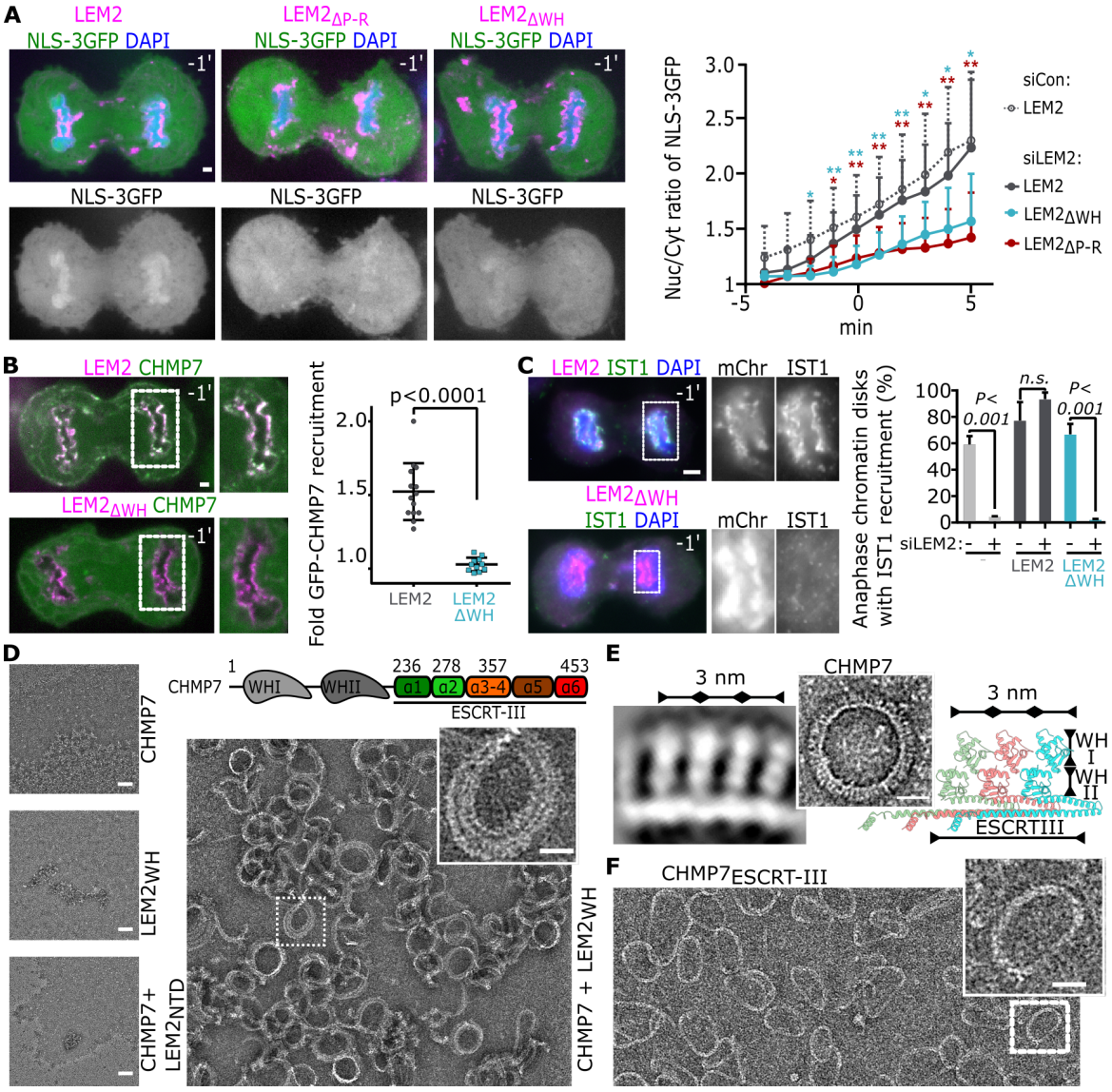

Fig. 3. LEM2's C-terminal WH domain induces CHMP7 polymerization and is required to compartmentalize the nascent NE.

(A) Left: Example images of cells treated with siLEM2 and expressing NLS-3GFP in combination with the indicated siRNA resistant LEM2-mChr constructs. Right: Mean ratio of nuclear/cytoplasmic NLS-3GFP throughout late anaphase. p-values are indicated as follows: $*P < 0.05$; $**P < 0.005$; N.S., not significant. Bars are SD. (B) Live cell imaging of LEM2-mChr or $LEM2_{\Delta WH}$ alongside GFP-CHMP7 in late anaphase. GFP-CHMP7 enrichment to regions of interest defined by LEM2-mChr or $LEM2_{\Delta WH}$-mChr localization is quantified. Bars are SD. (C) Left: Localization of endogenous IST1 in cells depleted of endogenous LEM2 and expressing the indicated siRNA resistant LEM2-mChr constructs. Right: Quantification of robust IST1 recruitment to chromatin disks in late anaphase. Error bars are SEM. Scale 2um A-C. (D) Top right: CHMP7 domain architecture. Left, right: Negative stain EM CHMP7 polymerization assay with indicated components. (E) High magnification 2D class average of polymerized CHMP7. Inset: Low-magnification polymerized ring of full-length CHMP7. Right: Homology model of polymeric CHMP7. (F) Negative stain EM of $CHMP7_{229\text{-}453}$. Scale 20 nm D-F.

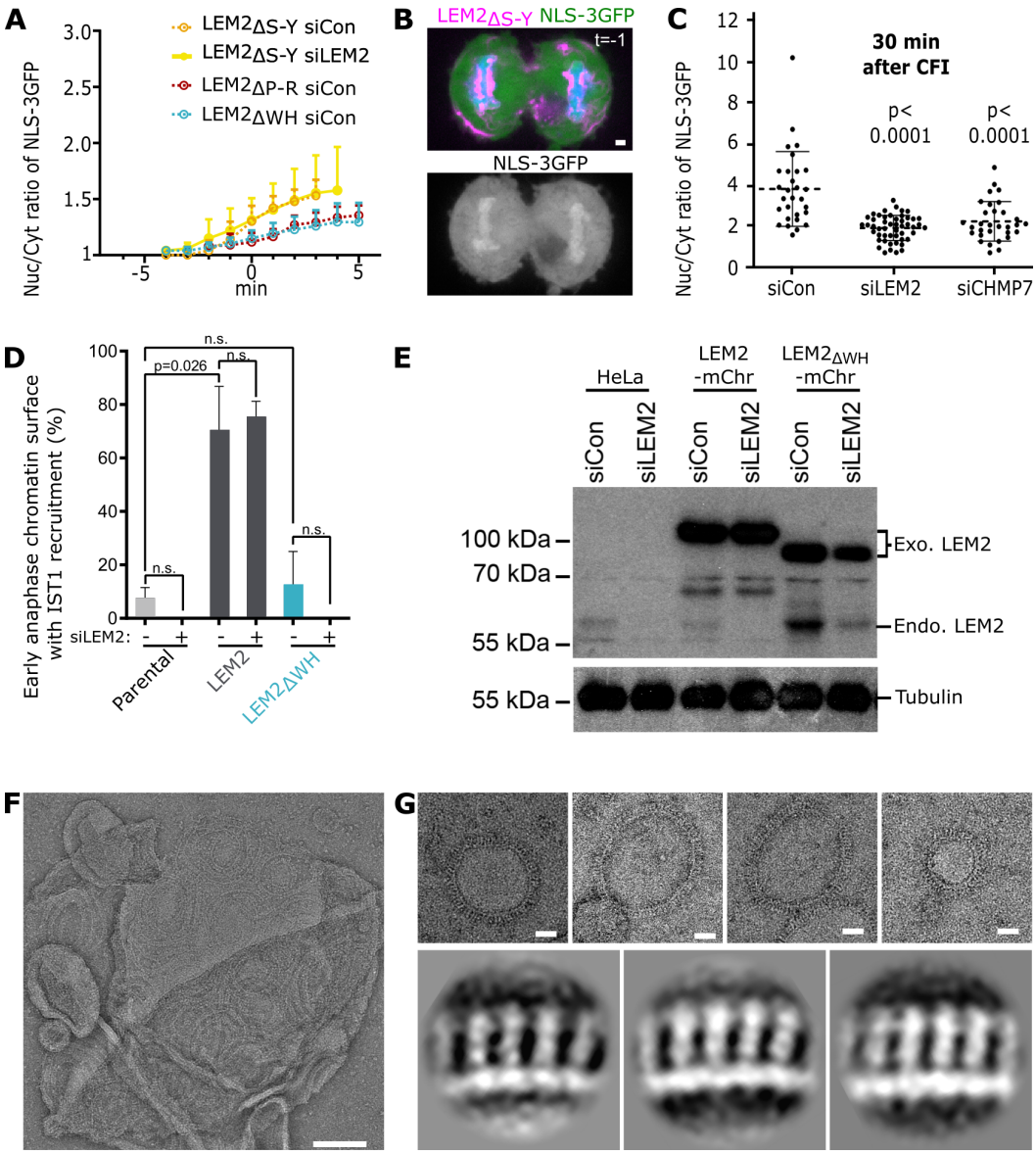

Extended Data Fig. 4. LEM2 promotes nuclear compartmentalization and IST1 recruitment via its WH domain and CHMP7 forms polymers on membrane.

(A) Quantification of the nuclear:cytoplasmic ratio of NLS-3GFP fluorescence over time in cells treated with the indicated siRNAs and expressing the indicated siRNA resistant constructs. (B) Example images of cells treated with siLEM2 and expressing NLS-3GFP in combination with siRNA resistant LEM2-$_{\Delta S\text{-}Y}$-mChr constructs. Scale 2 um. (C) Quantification of nuclear:cytoplasmic ratio of NLS-3GFP 30 minutes after complete cleavage furrow ingression in parental HeLa cells treated with the indicated siRNAs. (D) Quantification of the percent of early anaphase disks with robust IST1 recruitment, as assessed by blind scoring. Bars represent the average of three independent experiments and are graphed showing standard error of the mean. Student's t-test was used to determine p-values; N.S., not significant. (E) Immunoblot showing overexpression of the siRNA-resistant full length LEM2-mCherry (84kDa) and LEM2$_{\Delta WH}$-mChr (76kDa). Endogenous LEM2 is approximately 60kDa. (F) Negative stain EM of CHMP7 polymers on a liposome. Scale 100 nm. (G) Top: Negative stain EM of membrane-induced CHMP7 polymers used for 2D averaging. Scale 20 nm. Bottom: Representative 2D-class averages from manually particles from polymers shown in G.

Table 1. Quantification of IST1 recruitment in mammalian cells

IST1			Figure 3C - Late Anaphase				Extended Data Figure 4D - Early Anaphase			
			Exp 1	Exp 2	Exp 3	**Mean**	Exp 1	Exp 2	Exp 3	**Mean**
Parental	siControl	Extra*	18	0	0	**6**	5	0	0	**2**
		Robust	50	60	46	**52**	5	13	0	**6**
		Weak	11	38	34	**28**	0	50	35	**28**
		Absent	21	2	20	**14**	89	38	65	**64**
		n	80	58	106		38	16	20	
	siLEM2-2	Extra	0	0	0	**0**	0	0	0	**0**
		Robust	4	4	3	**4**	0	0	0	**0**
		Weak	37	36	67	**47**	0	0	8	**3**
		Absent	59	60	29	**49**	100	100	92	**97**
		n	78	50	58		24	10	25	
LEM2-mChr	siControl	Extra	61	93	21	**58**	32	90	38	**53**
		Robust	15	7	31	**18**	6	0	46	**17**
		Weak	17	0	29	**15**	8	10	17	**12**
		Absent	7	0	19	**9**	54	0	0	**18**
		n	46	42	62		50	20	24	
	siLEM2-2	Extra	77	94	40	**70**	53	86	75	**71**
		Robust	19	4	42	**22**	13	0	0	**4**
		Weak	4	2	11	**6**	13	0	25	**13**
		Absent	0	0	6	**2**	21	14	0	**12**
		n	78	51	62		38	14	8	
LEM2Δ415-485-mChr	siControl	Extra	0	0	12	**4**	0	0	0	**0**
		Robust	50	73	62	**62**	0	38	0	**13**
		Weak	38	27	26	**30**	9	6	20	**12**
		Absent	12	0	0	**4**	91	56	80	**76**
		n	138	52	42		44	16	20	
	siLEM2-2	Extra	0	0	0	**0**	0	0	0	**0**
		Robust	2	0	2	**1**	0	0	0	**0**
		Weak	15	13	49	**26**	0	0	21	**7**
		Absent	83	88	49	**73**	100	100	79	**93**
		n	112	48	51		20	4	14	

*Numbers reported are the percentage of chromatin discs scored as extra robust, robust, weak or absent for IST1. Although robust and extra robust were quantified as separate categories, they are graphed as a single category for clarity.

Table 2. Template Structures Used for Homology Modeling.

Protein	AAs covered by model	Template Structure	Model Organism	PDB Identifier
$CHMP7_{ESCRTIII}$ open	238-356	SNF7	*S.c.*	5FD7[41]
$CHMP7_{ESCRTIII}$ closed	235-373	CHMP3	*H.s.*	2GD5[80]
$CHMP7_{WH1 + WH2}$	42-223	VPS25	*H.S.*	3CUQ[29]
$LEM2_{WH}$	396-501	MAN1	*H.s.*	2CH0[39]

LEM2 and CHMP7 co-polymerize

To probe the mechanism of CHMP7 autoinhibition and release by $LEM2_{WH}$, we employed a quantitative isotopic labeling and cross-linking mass spectrometry (XL-MS) approach (**Fig. 4A, Table 3**). Labeling monomeric CHMP7 with a heavy crosslinker and $LEM2_{WH}$-induced polymers with a light crosslinker, we measured crosslink enrichment between samples. We identified 24 cross-links specific to monomeric CHMP7. Hybrid peptide mapping revealed that the N- and C-termini of CHMP7 fold back to interact with each other and with the α1-α3 helices of CHMP7's ESCRT-III domain (**Fig. 4A-B, and Extended Data 5A-F**). These interactions in the monodisperse CHMP7 dataset were significantly reduced or absent in $LEM2_{WH}$-induced CHMP7 polymers (**Fig. 4A-B, Extended Data Fig. 5 and Table 2**), consistent with a conformational change into an open and polymeric state, as visualized by EM (**Fig. 3D-F**). In total, 19 cross-links were enriched in the $LEM2_{WH}$-induced polymeric sample, mapping to interactions between $LEM2_{WH}$ and α1-α3 of CHMP7. Polymer-specific cross-links between N-terminal amines of neighboring CHMP7 molecules, and between adjacent $LEM2_{WH}$ subunits, are most consistent with copolymerization of both proteins (**Fig. 4A-B, Extended Data Fig. 5**). Corroborating the XL-MS, mutating conserved residues within CHMP7 α1-3—guided by the hybrid peptides between them—impaired $LEM2_{WH}$-CHMP7 co-polymerization as quantified in a co-pelleting assay (**Fig. 4C and D, Extended Data Fig. 5G**).

To further evaluate the stoichiometric ratio of LEM_{WH} and CHMP7 within these copolymers, we quantified CHMP7 polymerization with increasing concentrations of $LEM2_{WH}$ using the pelleting assay. We found that LEM2's WH domain activated CHMP7 through copolymerization in a 1:1 stoichiometric ratio, rather than seeding CHMP7 polymerization through nucleation (**Fig. 4E and F**). Interestingly,

CHMP7 polymerization is both activated and stoichiometrically limited by $LEM2_{WH}$, suggesting that LEM2 LCD-mediated condensation on MTs acts as a mechanism of enrichment, which promotes ESCRT-III activity. Further, these data indicate that autoinhibited CHMP7 is activated through a domain swap mechanism, whereby $LEM2_{WH}$ binds to the α1-3 region of CHMP7 to displace CHMP7's autoinhibitory VPS25-like WH domains. In the polymer conformation, this ESCRT-II-like region of CHMP7 is displaced from interactions with the ESCRT-III domain, and may thus become available for downstream ESCRT-III binding (**Fig. 3E, Fig. 4F**).

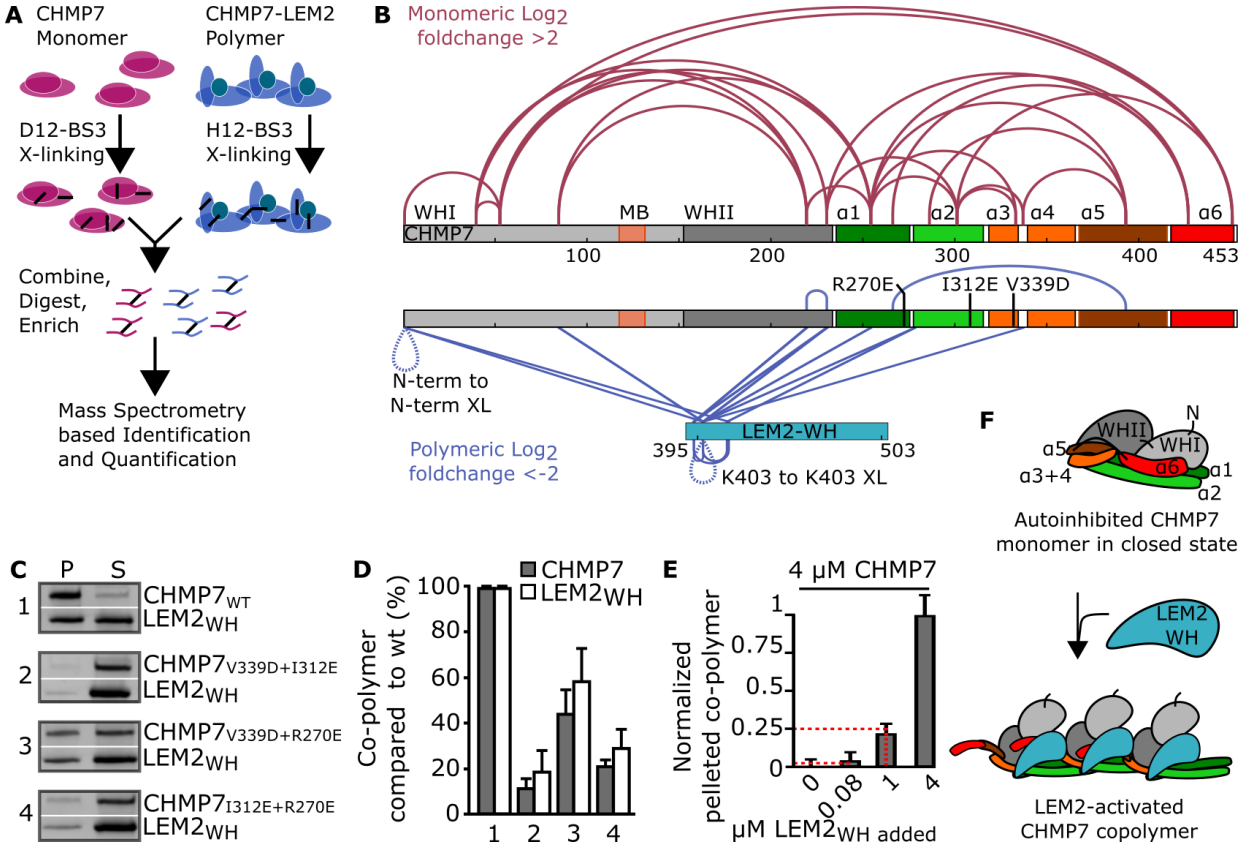

Fig. 4. The WH domain of LEM2 relieves CHMP7 autoinhibition to activate CHMP7 polymerization.

(A) Workflow of lysine-lysine hybrid peptide mapping using XL-MS. BS3 cross-links surface accessible Lys residues with Cα-Cα distances <~3nm. (B) Interactions that were enriched more than 4-fold are mapped on to the protein primary structure: enrichments in monomeric CHMP7 (red) or $LEM2_{WH}$-CHMP7 polymer (blue). Tested CHMP7 point mutations are indicated. MB, membrane binding. (C) SDS-PAGE of pellet (P) or supernatant (S) following centrifugation of $LEM2_{WH}$ incubated with wild type or mutant CHMP7. (D) Quantification of pelleted protein in mutant samples compared to WT, from SDS-PAGE in C. (E) SDS-PAGE based relative quantification of polymerized and pelleted CHMP7 with different ratios of $LEM2_{WH}$ present. Red lines indicate expected fraction of CHMP7 in the pelleted polymer, assuming 1:1 stoichiometric polymer. N=3. Error bars are SD. (F) Cartoon summary of LEM2-mediated CHMP7 activation.

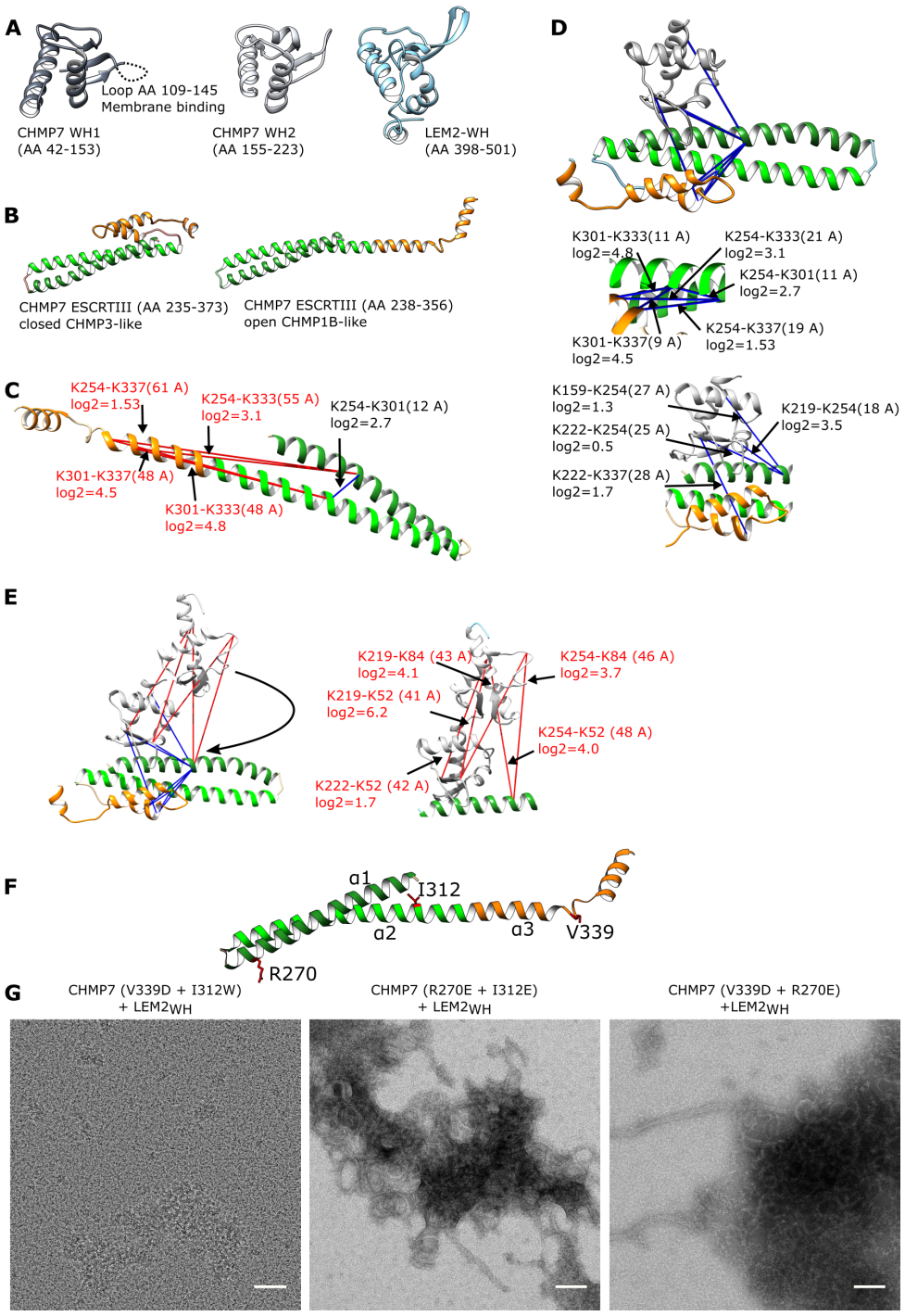

Extended Data Fig. 5. Homology modeling and crosslinking-mass spectrometry (XL-MS) reveal structural dynamics of CHMP7.

(A) Homology models for the winged helix (WH) domains of CHMP7 and LEM2. WH1 of CHMP7 contains a membrane binding region indicated as a loop[27]. (B) Homology models of the CHMP7 ESCRT-III-fold in open and closed confirmations. Alpha helices 1-2 (green), 3-4 (orange). (C) Distance restraints identified from XL-MS analysis of the CHMP7 monomer were mapped to open and closed homology models. Cα-Cα distances > 3 nm are considered violations. Satisfied restraints are show in blue, and

violated restraints are shown in red. The open ESCRTIII conformation was rejected. (D) Top: A crystallographic interface between VPS25 and an ESCRT-III helix [30] resembles the CHMP7 WHII interaction with the CHMP7 ESCRT-III domain. Middle and bottom: All cross-links are satisfied when mapped to the closed CHMP7-ESCRTIII model (middle and lower panel) and agree with domain connectivity. A subset of cross-links was not satisfied when mapping WH1 instead to same interface (data not shown). (E) Left: Distance restraints identified from XL-MS analysis of CHMP7 monomer mapped to conformation of polymerized CHMP7 consistent with 2D class averages. Satisfied restraints (blue), violated restraints (red). Violated restrains suggest a hinge region between CHMP7 WH1 and WH2 that allows its WH1 to move closer to the ESCRTIII core (black arrow). Right: Violated restrains to WH2 are indicated. (F) CHMP7 point mutations are indicated in an open ESCRT-III-fold, representing polymerized CHMP7. Color code from Fig. 4. (G) Negative stain EM of His_6-SUMO-$LEM2_{WH}$ co-incubated with CHMP7 mutants. Scale bars are 50 nm.

Table 3. Quantified Cross-links from comparative mass spectrometry analysis between monomeric CHMP7 and CHMP7 polymerized by $LEM2_{WH}$.

Summed peak areas for identified cross-links are listed for Heavy (polymeric CHMP7) and Light (Monomeric CHMP7). In case the identified cross-link was absent in Light sample, the value was set to 40000 for analysis purposes and the log2 ratio is shown as n/a. Cross-links with log2 ratios between 2 and -2 as well as cross-links falling into the region of the His6-SUMO-tag present in $LEM2_{WH}$ were filtered and not considered in the analysis.

Protein 1	Res	Protein 2	Res	Heavy	Light	log2 ratio	Comment
CHMP7	301	CHMP7	451	2.25E+09	40000	n/a	**monomeric**
CHMP7	451	CHMP7	52	7.68E+08	40000	n/a	**monomeric**
CHMP7	230	CHMP7	427	3.10E+08	40000	n/a	**monomeric**
CHMP7	254	CHMP7	427	7.82E+09	2176710	11.80997	**monomeric**
CHMP7	230	CHMP7	52	4.22E+09	48635490	6.437429	**monomeric**
CHMP7	219	CHMP7	52	4.05E+09	55869660	6.179847	**monomeric**
CHMP7	254	CHMP7	393	2.81E+09	56581520	5.633818	**monomeric**
CHMP7	219	CHMP7	39	2.94E+10	7.34E+08	5.32449	**monomeric**
CHMP7	301	CHMP7	333	2.05E+10	7.38E+08	4.794842	**monomeric**
CHMP7	301	CHMP7	337	8.61E+10	3.81E+09	4.497747	**monomeric**
CHMP7	219	CHMP7	84	9.45E+09	5.41E+08	4.127288	**monomeric**
CHMP7	286	CHMP7	393	3.72E+10	2.16E+09	4.108337	**monomeric**
CHMP7	254	CHMP7	52	2.63E+10	1.54E+09	4.09429	**monomeric**
CHMP7	254	CHMP7	84	7.94E+09	6.31E+08	3.653798	**monomeric**
CHMP7	230	CHMP7	301	1.21E+09	1.04E+08	3.540293	**monomeric**
CHMP7	219	CHMP7	254	4.29E+10	3.82E+09	3.489168	**monomeric**
CHMP7	39	CHMP7	52	1.04E+11	1.13E+10	3.197974	**monomeric**
CHMP7	254	CHMP7	39	2.73E+10	3.01E+09	3.184349	**monomeric**
CHMP7	254	CHMP7	333	2.08E+09	2.34E+08	3.151617	**monomeric**
CHMP7	266	CHMP7	427	5.47E+09	6.87E+08	2.993479	**monomeric**
CHMP7	254	CHMP7	301	9.92E+11	1.54E+11	2.682457	**monomeric**
CHMP7	39	CHMP7	451	1.63E+10	2.94E+09	2.470683	**monomeric**
CHMP7	337	CHMP7	393	1.16E+09	2.41E+08	2.267646	**monomeric**
CHMP7	0	CHMP7	52	6.88E+10	1.64E+10	2.068914	**monomeric**
CHMP7	0	CHMP7	39	2.43E+11	6.24E+10	1.959349	filtered

Protein 1	Res	Protein 2	Res	Heavy	Light	log2 ratio	Comment
CHMP7	0	CHMP7	301	2.31E+09	6.80E+08	1.764613	filtered
CHMP7	222	CHMP7	337	4.16E+09	1.25E+09	1.738456	filtered
CHMP7	266	CHMP7	440	1.49E+08	45128460	1.727354	filtered
CHMP7	222	CHMP7	52	1.12E+10	3.42E+09	1.71803	filtered
CHMP7	206	CHMP7	230	4.21E+09	1.44E+09	1.542644	filtered
CHMP7	254	CHMP7	337	1.25E+11	4.33E+10	1.529526	filtered
CHMP7	427	CHMP7	451	7.24E+09	2.81E+09	1.368246	filtered
CHMP7	0	CHMP7	230	8.14E+10	3.24E+10	1.328587	filtered
CHMP7	159	CHMP7	254	1.86E+09	7.55E+08	1.296796	filtered
CHMP7	440	CHMP7	451	1.47E+11	6.25E+10	1.232975	filtered
CHMP7	230	CHMP7	393	2.75E+08	1.32E+08	1.057213	filtered
CHMP7	0	CHMP7	393	9.15E+09	4.44E+09	1.042463	filtered
CHMP7	0	CHMP7	219	1.13E+11	5.58E+10	1.012006	filtered
CHMP7	0	CHMP7	159	2.83E+09	1.40E+09	1.010835	filtered
CHMP7	278	CHMP7	427	5.48E+09	2.73E+09	1.005542	filtered
CHMP7	254	CHMP7	451	7.64E+10	3.88E+10	0.978914	filtered
CHMP7	301	CHMP7	393	1.08E+09	5.60E+08	0.944398	filtered
CHMP7	393	CHMP7	427	2.56E+08	1.49E+08	0.775447	filtered
CHMP7	222	CHMP7	254	2.78E+10	1.98E+10	0.492327	filtered
CHMP7	0	CHMP7	278	1.18E+09	8.90E+08	0.404775	filtered
CHMP7	230	CHMP7	254	5.93E+10	5.40E+10	0.134532	filtered
CHMP7	337	CHMP7	451	4.33E+09	4.20E+09	0.045864	filtered
CHMP7	254	$LEM2_{395-503}$	Tag	40000	40000	0	filtered
CHMP7	0	CHMP7	427	1.94E+09	2.31E+09	-0.24955	filtered
CHMP7	278	CHMP7	451	2.67E+10	3.47E+10	-0.38233	filtered
CHMP7	393	CHMP7	451	9.74E+09	1.29E+10	-0.40201	filtered
CHMP7	278	CHMP7	286	9.30E+10	1.42E+11	-0.61524	filtered
CHMP7	393	CHMP7	440	4.21E+09	6.58E+09	-0.64225	filtered
CHMP7	0	CHMP7	451	1.08E+10	1.73E+10	-0.68019	filtered
CHMP7	230	CHMP7	337	2.40E+09	4.05E+09	-0.75357	filtered
CHMP7	254	CHMP7	440	1.22E+10	2.23E+10	-0.86908	filtered
CHMP7	266	CHMP7	278	7.01E+09	1.56E+10	-1.15414	filtered
CHMP7	278	CHMP7	443	39489130	1.01E+08	-1.34783	filtered
CHMP7	278	CHMP7	440	2.98E+09	8.53E+09	-1.51962	filtered
CHMP7	0	CHMP7	254	4.31E+08	1.27E+09	-1.55312	filtered
CHMP7	337	CHMP7	440	3.15E+08	9.42E+08	-1.58103	filtered
CHMP7	0	CHMP7	337	6.76E+09	2.08E+10	-1.62117	filtered
CHMP7	278	CHMP7	393	4.86E+08	1.81E+09	-1.89367	filtered
CHMP7	0	CHMP7	440	1.97E+08	7.50E+08	-1.92841	filtered

Protein 1	Res	Protein 2	Res	Heavy	Light	log2 ratio	Comment
$LEM2_{395-503}$	416	CHMP7	278	1.37E+08	9.53E+08	-2.8037	**polymeric**
$LEM2_{395-503}$	403	$LEM2_{395-503}$	416	48069950	3.64E+08	-2.91974	**polymeric**
$LEM2_{395-503}$	403	CHMP7	254	79126185	1.03E+09	-3.70433	**polymeric**
CHMP7	219	CHMP7	230	5.57E+09	7.68E+10	-3.78607	**polymeric**
$LEM2_{395-503}$	Tag	$LEM2_{395-503}$	Tag	44794046	6.27E+08	-3.80764	filtered
$LEM2_{395-503}$	403	$LEM2_{395-503}$	403	1.73E+08	2.98E+09	-4.10901	**polymeric**
$LEM2_{395-503}$	398	CHMP7	219	12906998	2.49E+08	-4.27046	**polymeric**
CHMP7	0	$LEM2_{395-503}$	417	25789106	5.01E+08	-4.28097	**polymeric**
$LEM2_{395-503}$	416	$LEM2_{395-503}$	Tag	1.17E+09	2.79E+10	-4.57714	filtered
$LEM2_{395-503}$	403	CHMP7	337	3489515	86905840	-4.63835	**polymeric**
$LEM2_{395-503}$	403	$LEM2_{395-503}$	Tag	7.22E+08	2.30E+10	-4.99053	filtered
CHMP7	0	$LEM2_{395-503}$	403	1.66E+08	6.48E+09	-5.29086	**polymeric**
$LEM2_{395-503}$	403	$LEM2_{395-503}$	417	4.01E+08	1.64E+10	-5.35557	**polymeric**
CHMP7	39	$LEM2_{395-503}$	Tag	10022825	4.28E+08	-5.41505	filtered
CHMP7	278	$LEM2_{395-503}$	Tag	33962780	1.73E+09	-5.67172	filtered
$LEM2_{395-503}$	417	$LEM2_{395-503}$	Tag	1.33E+08	7.31E+09	-5.78185	filtered
$LEM2_{395-503}$	398	$LEM2_{395-503}$	417	43637149	2.79E+09	-5.99857	**polymeric**
CHMP7	0	CHMP7	0	9958810	7.52E+08	-6.23788	**polymeric**
$LEM2_{395-503}$	417	$LEM2_{395-503}$	Tag	45397140	5.06E+09	-6.7994	filtered
CHMP7	266	CHMP7	393	81110700	9.15E+09	-6.81778	**polymeric**
$LEM2_{395-503}$	Tag	CHMP7	451	24592260	2.94E+09	-6.89985	filtered
$LEM2_{395-503}$	403	CHMP7	278	7117124	1.04E+09	-7.18667	**polymeric**
$LEM2_{395-503}$	403	$LEM2_{395-503}$	Tag	1.57E+09	3.00E+11	-7.57701	filtered
$LEM2_{395-503}$	398	$LEM2_{395-503}$	403	1.17E+09	2.77E+11	-7.88329	**polymeric**
CHMP7	0	$LEM2_{395-503}$	Tag	7275826	1.78E+09	-7.93108	filtered
CHMP7	0	$LEM2_{395-503}$	Tag	7275826	1.78E+09	-7.93108	filtered
CHMP7	337	$LEM2_{395-503}$	Tag	9596912	2.58E+09	-8.06835	filtered
$LEM2_{395-503}$	Tag	$LEM2_{395-503}$	Tag	900147	2.62E+08	-8.18409	filtered
$LEM2_{395-503}$	403	CHMP7	230	3359563	1.50E+09	-8.80112	**polymeric**
$LEM2_{395-503}$	398	$LEM2_{395-503}$	416	35615163	1.87E+10	-9.03936	**polymeric**
$LEM2_{395-503}$	Tag	$LEM2_{395-503}$	Tag	3585642	1.97E+09	-9.10148	filtered
$LEM2_{395-503}$	Tag	$LEM2_{395-503}$	Tag	1.94E+09	1.08E+12	-9.12388	filtered
$LEM2_{395-503}$	398	$LEM2_{395-503}$	Tag	5.34E+08	4.03E+11	-9.56121	filtered
CHMP7	0	$LEM2_{395-503}$	Tag	30515594	3.61E+10	-10.2098	filtered
CHMP7	219	$LEM2_{395-503}$	Tag	3239630	6.50E+09	-10.9706	filtered
$LEM2_{395-503}$	403	CHMP7	84	40000	89168505	-11.1223	**polymeric**

Protein 1	**Res**	**Protein 2**	**Res**	**Heavy**	**Light**	**log2 ratio**	**Comment**
CHMP7	337	$LEM2_{395-503}$	Tag	3413843	8.26E+09	-11.2398	filtered
$LEM2_{395-503}$	Tag	$LEM2_{395-503}$	403	40000	1.42E+08	-11.791	filtered
$LEM2_{395-503}$	Tag	CHMP7	254	1298693	8.01E+09	-12.5914	filtered
$LEM2_{395-503}$	Tag	CHMP7	0	80000	7.79E+08	-13.2486	filtered
CHMP7	337	$LEM2_{395-503}$	Tag	40000	5.61E+08	-13.7757	filtered
$LEM2_{395-503}$	398	CHMP7	230	491619	1.00E+10	-14.3161	**polymeric**
CHMP7	0	$LEM2_{395-503}$	Tag	40000	1.08E+10	-18.0449	filtered

Loss of LEM2 function prevents spindle clearance and disrupts nuclear integrity.

Prior work has shown that extended siRNA-mediated LEM2 depletion causes a nuclear malformation phenotype in interphase and is eventually lethal[34]. To identify whether nuclear morphology defects arise at mitotic exit, we synchronized cells following LEM2 depletion and imaged their progression from anaphase to late telophase. While LEM2-depleted cells progressed to anaphase without noticeable nuclear defects, a strong nuclear and tubulin-morphology phenotype began to emerge in late anaphase and persisted through telophase (**Fig. 5A**). An orthogonal view of the LEM2-depletion phenotype revealed that aberrant MT bundles could be seen tunneling through the nucleus within a channel lined by nuclear membrane (**Extended Data Fig. 6A and B**). The appearance of DNA damage in telophase U2OS cells depleted of LEM2, a hallmark of defective nuclear integrity, underscores the significance of these nuclear morphology phenotypes (**Fig. 5B**).

To evaluate still later phenotypes, we depleted endogenous LEM2 in cells stably expressing siRNA-resistant LEM2-, $LEM2_{\Delta P\text{-}R}$- or $LEM2_{\Delta WH}$-mChr while concurrently arresting them in S phase. Consequently, after progression through one round of division, we observed an increased number of highly irregular nuclei in cells expressing either $LEM2_{\Delta P\text{-}R}$-mChr or $LEM2_{\Delta WH}$-mChr compared to cells expressing full-length LEM2 or even those depleted of LEM2 (**Fig. 5C**). Notably, deformed nuclei were commonly associated with microtubule disorganization and aberrant accumulation of $LEM2_{\Delta P\text{-}R}$-mChr and $LEM2_{\Delta WH}$-mChr **(Fig. 5C, Extended Data 6C**). These findings suggest that interfering with cooperation between LEM2's microtubule-interacting and ESCRT-binding domains leads to gross alterations in nuclear morphology, indicating that both activities are necessary, but neither is sufficient, for nuclear envelope reformation in vivo. Moreover, the presence of one activity without the other is detrimental to nuclear morphology.

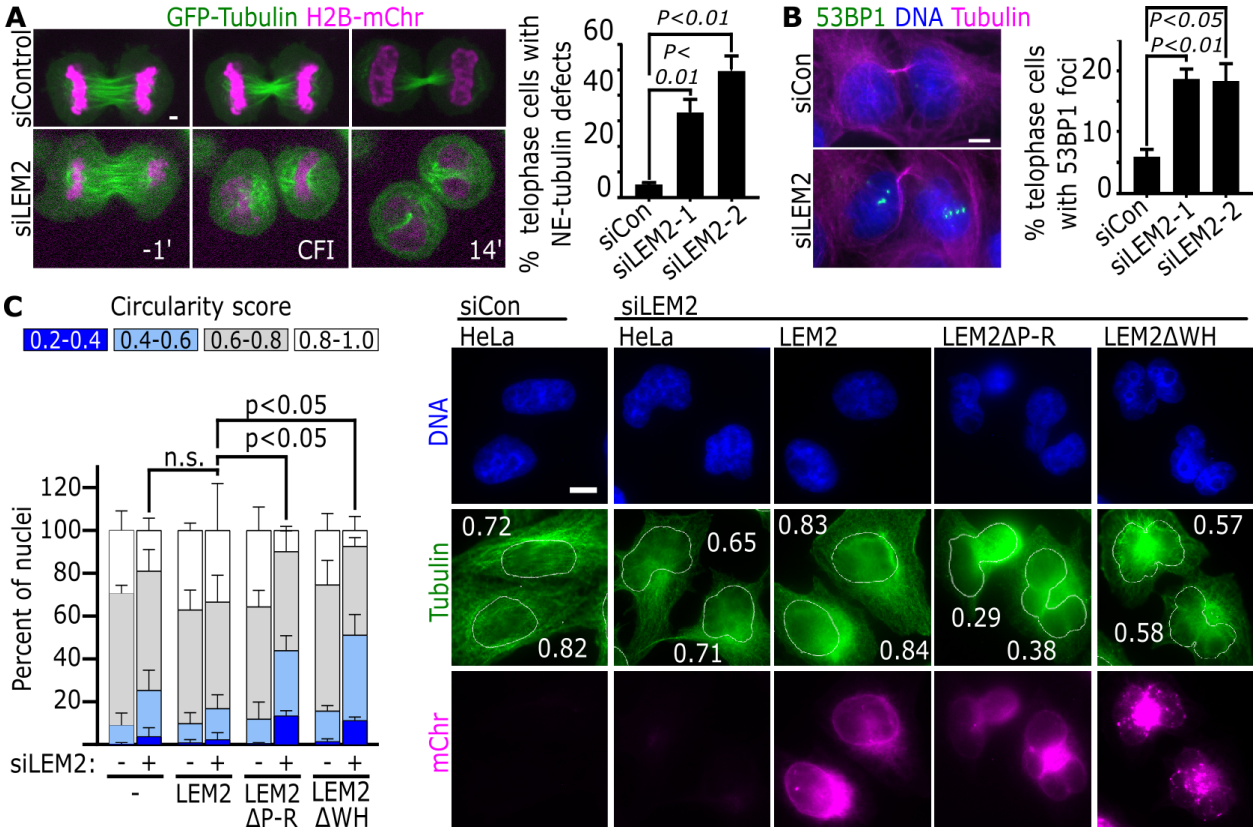

Fig. 5. Coordination of the ESCRT-III pathway by LEM2 is critical for timely spindle disassembly and post-mitotic genome integrity.

(A) Left: Live-cell imaging of GFP-tubulin and H2B-mChr in siRNA treated cells. Time 0 refers to complete cleavage furrow ingression. Right: Tubulin defect scoring in telophase cells. Error bars are SEM. (B) Left: Example images of 53BP1 localization in telophase U2OS cells following siRNA treatment. Right: Graph shows percent of telophase cells with ≥5 53BP1 foci. Error bars are SEM. (C) Left: Quantification of interphase nuclear circularity in parental HeLa cells and cells expressing the indicated siRNA-resistant constructs following siRNA treatment. Bars are SEM; P-values between circularity bins indicated in blue; N.S., not significant Right: Example images of interphase cells with the nuclear, tubulin, and LEM2-mChr localization defects observed when LEM2 is depleted, compared to siControl-treated parental HeLa cells. Nuclear borders and circularity scores are annotated in tubulin channel. Scale 2 um A-C.

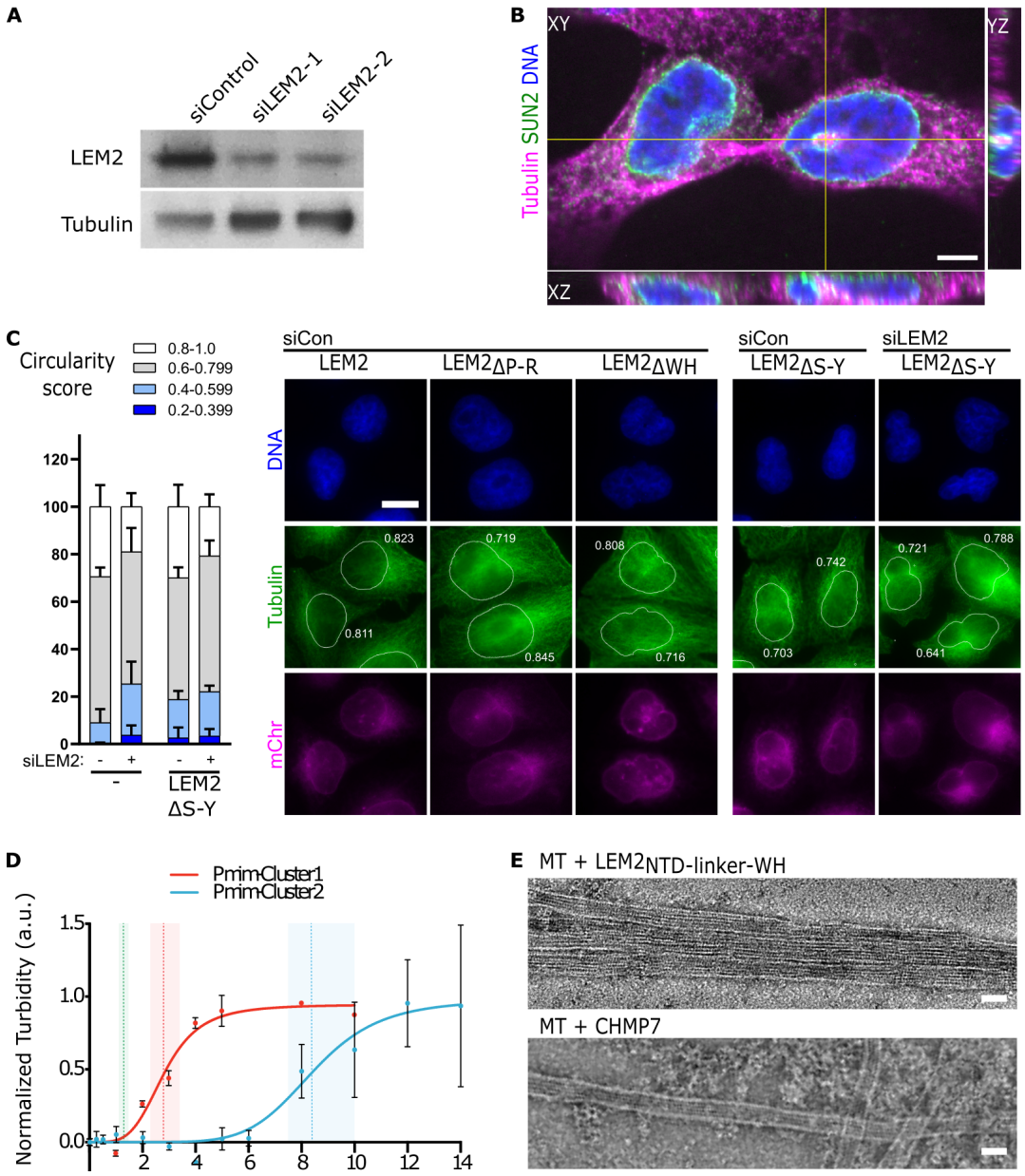

Extended Data Fig. 6. LEM2 promotes proper nuclear morphology and is phosphoregulated via its low complexity domain.

(A) Immunoblot indicating level of LEM2 depletion by two independent siRNAs in U2OS cells. (B) Orthogonal view of the tubulin phenotype following LEM2 depletion co-stained for the INM protein SUN2. Scale 2 um. (C) Left: Quantification of nuclear circularity in interphase parental HeLa cells (data duplicated from Figure 5) and cells expressing LEM2 $_{\Delta S\text{-}Y}$ -mChr and treated with the indicated siRNAs. Bars are SEM. Right: Example images of interphase cells expressing the indicated siRNA-resistant constructs and treated with the indicated siRNAs. Nuclear borders and circularity scores annotated in tubulin channel. Scale 2 um. (D) Light scattering quantification of microtubule bundling by phosphomimetic LEM2 constructs. Vertical lines are half max and shading is standard error; LEM2$_{NTD}$ (green), LEM2$_{Cluster1}$ (red), LEM2$_{Cluster2}$ (blue). (E) Negative stain EM of indicated combinations of MT, LEM2$_{NTD\text{-}linker\text{-}WH}$, and CHMP7$_{FL}$. Scale 25 nm.

LEM2 LCD is mitotically phosphoregulated for timely NE reformation in anaphase.

Given that LEM2 coordinately phase separates into liquid-like states, binds MTs, and activates CHMP7 to promote compartmentalization at the nascent NE, we sought to address how the cell patterns these functions in space and time, particularly in the context of open mitosis in mammalian cells. LEM2 has several annotated phosphosites within the LCD[42]. To test whether phosphorylation of LEM2 could be a regulatory mechanism, we arrested cells in G1/S versus mitosis and probed the phosphorylation status of LEM2 by immunodetection following protein separation using "phos-tag" SDS-PAGE[43]. We found that LEM2-mChr is heavily phosphorylated in mitosis, compared to G1/S (Fig 6A and B). Treatment of mitotic cell lysate with phosphatase collapsed LEM2 bands, verifying that the ladder of LEM2 species corresponds to phosphorylated LEM2. We further compared deletion-mutants to full-length protein and found, in contrast, that the LCD domain-deletion constructs $LEM2_{\Delta S\text{-}Y}$-mChr and $LEM2_{\Delta P\text{-}R}$-mChr had simpler migration patterns, suggesting that mitotic phosphosites lie within those regions. Phosphomimetic mutations spanning the phase-separating S-Y-rich motif did not affect MT bundling activity of recombinant $LEM2_{NTD}$ in vitro, while phosphomimetic mutations spanning the MT-interacting P-R-rich motif and its flanking region impaired MT bundling (**Fig. 6D Extended Data Fig. 6D**). Importantly, neither phosphomimetic mutant formed droplets near the physiological regime (**Fig. 6C**)—suggesting that cell-cycle dependent phosphorylation events govern LEM2's ability to undergo liquid-like phase separation.

Finally, to test the central hypothesis that LEM2's LCD and WH activities cooperate with CHMP7 to self-assemble around spindle MTs, we engineered a simplified LEM2 construct bearing the extra-lumenal domains of LEM2 connected by a flexible linker, $LEM2_{NTD\text{-}LINKER\text{-}WH}$. This protein was soluble and purified as a monodisperse monomer under high ionic strength conditions. Strikingly, in the presence of monomeric, full-length CHMP7, and upon exchange into a physiological solution, $LEM2_{NTD\text{-}LINKER\text{-}WH}$ triggered CHMP7 copolymerization, and the resulting rings could be seen looping at and around small MT bundles (**Fig. 6E, Extended Data 6E**).

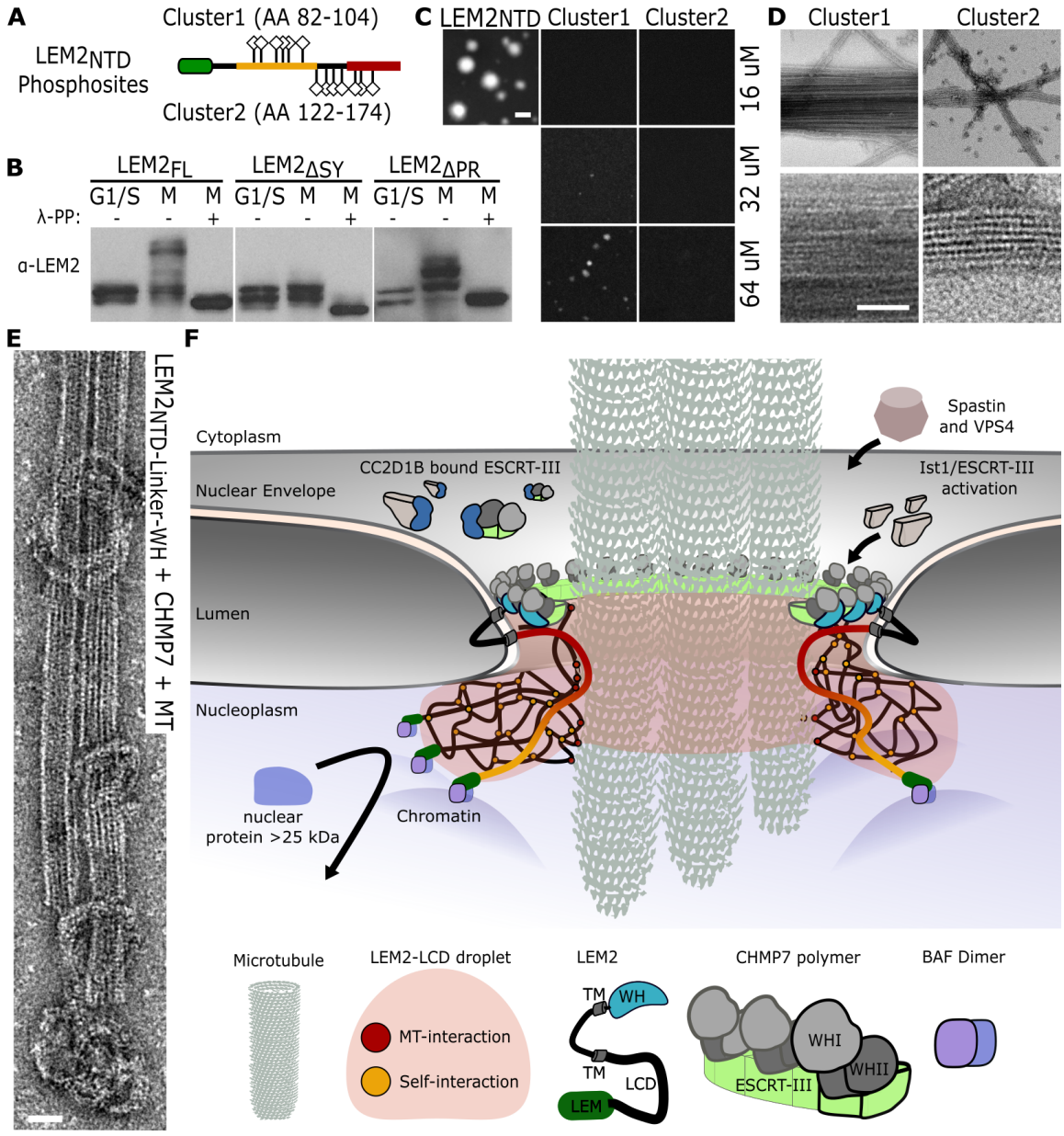

Fig. 6. LEM2 is phospho-regulated via its LCD.

(A) Schematic indicating sites of LEM2 phosphomimetic mutations. (B) LEM2 immunoblot assessing the migration pattern of full length and mutant LEM2-mChr following separation by Phos-tag SDS-PAGE. Cell lysates were prepared from G1/S- and mitotic- arrested cells expressing the indicated exogenous LEM2; lysates treated with lambda phosphatase (λ-PP) is indicated. (C) Fluorescence imaging of purified $LEM2_{NTD}$ and $LEM2_{NTD}$-phosphomimetic constructs (cluster 1 or cluster 2). Scale 2um. (D and E) Negative stain EM of co-incubated indicated proteins with MTs. Scale 25 nm. (F) Model of a molecular O-ring formed by LEM2 and CHMP7 during nuclear reformation that is required for spindle disassembly and to seal the nascent NE.

Discussion

In this work, we show how liquid-like phase separation underlies LEM2's function as an ESCRT-III adaptor during mitotic NE reformation. Our data are consistent with LEM2 and BAF dephosphorylation during the mitotic exit program when, together, these proteins begin coating the chromatin surface with LEM2-embedded membranes[3,4,6]. Through direct microtubule binding, LEM2 then concentrates in the core region of the anaphase nuclear envelope, where the LEM2 LCD mediates condensation into a liquid-like phase that wets the anionic surface of spindle MTs, similar to MAPT (Tau)[44,45]. MT wetting by membrane-embedded LEM2 could, therefore, draw the nascent NE around the residual MTs at these sites. Concentrated LEM2 then recruits cytoplasmic CHMP7, and together they self-assemble into polymers that are anchored by LEM2's integral connection to the membrane, encircling spindle MTs. All of these functions contribute to early nuclear compartmentalization during anaphase. We, therefore, propose that LEM2 and CHMP7 collaborate to form a molecular "O-ring" that establishes a temporary barrier between the new nucleoplasm and the cytoplasm before complete spindle disassembly and membrane fusion (Fig. 6F). Future work will address the importance of this environment for downstream ESCRT-dependent activities, including the disassemblase activities of VPS4 and SPASTIN[9,17,23,24].

Microtubule binding and PR-rich LCDs have been reported to drive protein phase transition through low-affinity and multi-valent electrostatic and cation–pi interactions in other contexts, and defects in these phenomena disrupt spatiotemporal cellular organization[31,37,38,44,46,47]. LEM2 is a disease-associated protein, with point mutations linked to human heart disease, cataracts, and progeria[14,48,49]. As we showed previously in fission yeast, deregulated LEM2-CHMP7 activity strongly distorts nuclear morphology and integrity[17]. Our new data provide insight into the range of abnormalities that result from deregulated LEM2-CHMP7 function in human cells—including failed spindle disassembly, loss of nuclear integrity, and DNA damage—which likely underlie disease phenotypes. LEM2 and CHMP7 may also play toxic roles during micronucleation and, therefore, be contributing factors in tumorigenesis[12,18,25].

LEM2's ability to undergo liquid-like phase separation, moreover, may be a determinant of its interphase functions as well—including regulated gene expression and MT-independent repair of damaged nuclei[50–55]. Our observation that other polyanions, like DNA and RNA, promote LEM2 condensation suggests that MTs are sufficient but may not be necessary for this phenomenon. Since many members of the LEM domain family contain an LCD between the LEM domain and the first transmembrane helix, their roles in gene expression may emerge from their ability to localize certain chromatin regions, which can also exist in phase-separated states, to the periphery of the nuclear envelope[56].

In summary, these data provide a novel perspective on how both the function and toxicity of the LEM2-CHMP7 pathway arise from their biochemical properties. Proper reformation of the nucleus depends on liquid-like phase separation by an integral membrane protein, a protein that is also responsible for recruiting and copolymerizing with the ESCRT-III machinery. Together, this partnership contributes to the emerging notion that phase separating domains found in transmembrane and membrane-associated proteins play critical roles in membrane biology more generally[57–61].

Methods

Table 4. Plasmids and cell lines used in this study.

Cell lines stably expressing exogenous, fluorescently labeled proteins were generated by transfecting parental HeLa cells with the described plasmids using Lipofectamine LTX Plus (Thermo Fisher) for 24 h before selection with the specified antibiotics

Plasmids					
ID	Construct	Vector and Source	Protein	Tag	Expression System
PL1	$CHMP7_{229-453}$	pCA528	CHMP7	His_6-SUMO	*E. coli*
PL2	CHMP7	pCA528	CHMP7	His_6-SUMO	*E. coli*
PL3	$CHMP7_{R270E + I312E}$	pCA528	CHMP7	His_6-SUMO	*E. coli*
PL4	$CHMP7_{R270E + V339D}$	pCA528	CHMP7	His_6-SUMO	*E. coli*
PL5	$CHMP7_{I312E + V339D}$	pCA528	CHMP7	His_6-SUMO	*E. coli*
PL6	$LEM2_{1-72}$	pCA528	LEM2	His_6-SUMO	*E. coli*
PL7	$LEM2_{1–208}$	pCA528	LEM2	His_6-SUMO	*E. coli*
PL7a	$LEM2_{Cluster1}$ (S82D, S90D, S96D, Y98D, T100D, Y104D),	pCA528	LEM2	His_6-SUMO	*E. coli*
PL7b	$LEM2_{Cluster2}$ (Y122D, S134D, S138D, S139D, T147D, S166D, S174D, S175D)	pCA528	LEM2	His_6-SUMO	*E. coli*
PL7c	LEM2	pCA528	LEM2	His_6-SUMO	*E. coli*
PL8	$LEM2_{395–503}$	pCA528	LEM2	His_6-SUMO	*E. coli*
PL10	$LEM2_{1-208-LINKER-395-503}$	pCA528	LEM2	His_6-SUMO	*E. coli*
PL11	BAF	pCA528	BAF	His_6-SUMO	*E. coli*
PL12	siRNA resistant GFP-CHMP7	From pMGF18[17]	CHMP7	GFP	Mammalian
PL13	siRNA resistant LEM2-mCherry	From pMGF196[17]	LEM2	mCherry	Mammalian
PL14	siRNA resistant LEM2m21-mCherry	From PL13	LEM2	mCherry	Mammalian
PL15	siRNA resistant $LEM2_{\Delta LCD(43-202)}$-mCherry	From PL13	LEM2	mCherry	Mammalian
PL16	siRNA resistant $LEM2_{\Delta S-Y(75-123)}$-mCherry	From PL13	LEM2	mCherry	Mammalian
PL17	siRNA resistant $LEM2_{\Delta P-R(145-213)}$-mCherry	From PL13	LEM2	mCherry	Mammalian
PL18	siRNA resistant $LEM2_{\Delta WH(415-485)}$-mCherry	From PL13	LEM2	mCherry	Mammalian
PL19	eGFP-BAF	From pLX304 (from DNASU) and EGFP-C1 backbone	BAF	GFP	Mammalian
PL20	NLS-3xGFP	Gift from Martin Hetzer	3xGFP	NLS	Mammalian
PL21	GFP-Lamin B2		LaminB2	GFP	Mammalian

Stable Cell Lines			
Expressed constructs	Plasmid used	Parental cell line	Selection
GFP-Tubulin + H2B-mCherry	Generated previously[78]		G418, Puromycin
GFP-CHMP7	PL12	HeLa	G418
LEM2-mChr	PL13	HeLa	Puromycin
$LEM2_{\Delta S\text{-}Y(75\text{-}123)}$-mChr	PL16	HeLa	Puromycin
$LEM2_{\Delta P\text{-}R(145\text{-}213)}$-mChr	PL17	HeLa	Puromycin
$LEM2_{\Delta WH(415\text{-}485)}$-mChr	PL18	HeLa	Puromycin
GFP-BAF + LEM2-mChr	PL13 and PL19	HeLa	G418, Puromycin
NLS-3xGFP and LEM2-mChr	PL20 and PL13	HeLa	G418, Puromycin
NLS-3xGFP and $LEM2_{\Delta S\text{-}Y(75\text{-}123)}$-mChr	PL20 and PL16	HeLa	G418, Puromycin
NLS-3xGFP and $LEM2_{\Delta P\text{-}R(145\text{-}213)}$-mChr	PL20 and PL17	HeLa	G418, Puromycin
NLS-3xGFP and $LEM2_{\Delta WH(415\text{-}485)}$-mChr	PL20 and PL18	HeLa	G418, Puromycin
LEM2-mChr and GFP-Lamin B2	PL13 and PL21	HeLa	G418, Puromycin

Cytoskeletal proteins

Porcine brain Tubulin reagents were purchased from Cytoskeleton, Inc., including unpolymerized Tubulin (T238P), unpolymerized, HiLyte-647-labeled Tubulin (TL670M), and pre-formed microtubules (MT002).

Purification of His_6-SUMO-tagged proteins

All purified proteins in this study, except full length LEM2, were expressed in a pCA528 vector (WISP08-174; DNASU Plasmid Repository) in BL21-(DE3)-RIPL *Escherichia coli* cells using an N-terminal His_6-SUMO affinity tag as described previously[17]. Full length LEM2 was expressed in a pCA528 vector in C43(DE3) *Escherichia coli* cells using an N-terminal His_6-SUMO affinity tag. All plasmids are listed in Table 4. Expression cultures (3- to 4-liter) were grown in ZY-5052 rich auto-induction media containing kanamycin, shaking (220 rpm) for 3 hours at 37°C, then overnight at 19°C. Cells were harvested by centrifugation.

Purification of BAF: Purification of full length, human BAF protein (Uniprot ID O75531) was adapted from a published protocol[7]. The purification was performed exactly as described, except His_6-SUMO-BAF was cleaved with His_6-Ulp1 protease (30 min, room temperature) to suit the use of the His_6-SUMO

affinity tag. Ultimately, Superdex 75 16/60 fractions containing BAF dimer were pooled, concentrated, and flash frozen in liquid nitrogen and stored as single use aliquots at -80°C.

Purification of LEM2 proteins: Protein constructs originating from the human LEMD2 protein (Uniprot ID Q8NC56), including $LEM2_{1\text{-}72}$, $LEM2_{NTD(1–208)}$, $LEM2_{Cluster1(S82D,\ S90D,\ S96D,\ Y98D,\ T100D,\ Y104D)}$, $LEM2_{Cluster2(Y122D,\ S134D,\ S138D,\ S139D,\ T147D,\ S166D,\ S174D,\ S175D)}$, $LEM2_{WH(395–503)}$, and $LEM2_{NTD(1\text{-}208)\text{-}LINKER\text{-}WH(395\text{-}503)}$ (linker sequence SAAGTGAGSGSAAS), were purified as follows. Harvested cells were resuspended in lysis buffer (5 mL per gram cell pellet) containing 5% glycerol, 10 mM imidazole, pH 8.0, 2 µg/mL DNase1, lysozyme and protease inhibitors, with HEPES and KCl concentrations optimized individually for each LEM2 protein construct (20 mM HEPES, pH 7.0, 500 mM KCl for $LEM2_{1\text{-}72}$ and $LEM2_{NTD\text{-}LINKER\text{-}WH}$, and 40 mM HEPES, pH 8.0, 350 mM KCl for $LEM2_{WH}$, $LEM2_{Cluster1}$ and $LEM2_{Cluster2}$). Cells were lysed by sonication on ice, and clarified (10,000g, 30 min, 4°C). Clarified lysate was incubated with Ni-NTA agarose resin (Qiagen) (4 mL bed volume, 1.5 h, 4°C), washed extensively with lysis buffer, and protein was eluted with 5 column volumes of lysis buffer supplemented with 350 mM imidazole, pH 8.0. Eluate was spin-concentrated (Vivaspin 20, 3KDa MWCO, PES) to 5 mL, and dialyzed overnight at 4°C into storage buffer (20 – 40 mM HEPES, pH 7.0 – 8.0, 5% glycerol), with KCl concentrations optimized individually per construct (300 mM for $LEM2_{1\text{-}72}$, 500 mM for $LEM2_{NTD\text{-}LINKER\text{-}WH}$, and 350 mM for $LEM2_{WH}$ and $LEM2_{Cluster1}$, 110 mM for $LEM2_{Cluster2}$). The His_6-SUMO tag was cleaved by incubation with His_6-Ulp1 protease during dialysis. LEM2 proteins were further purified by size exclusion chromatography using the Superdex 75 16/60 column (GE Life Sciences) in storage buffer, and LEM2-containing fractions were pooled, spin-concentrated (Vivaspin 6 3KDa MWCO, PES), and aliquoted.

$LEM2_{NTD}$ was purified similarly, including an additional preparative phase separation step. All steps were carried out at room temperature unless otherwise noted. Harvested cells were resuspended in lysis buffer (30 mM HEPES, pH 7.4, 500 mM KCl, 5% glycerol, 10 mM imidazole, pH 8.0, 2 µg/mL DNase1, lysozyme and protease inhibitors), and lysed by sonication with intermittent chilling on ice. Lysate was clarified by centrifugation (10,000g, 30 min), incubated with Ni-NTA agarose resin (4 mL bed volume, 1.5 h, room temperature), and washed extensively with lysis buffer. Protein was eluted with

lysis buffer supplemented with 350 mM imidazole, pH 8.0. Droplet formation was induced to enrich for His_6-SUMO-$LEM2_{NTD}$: the imidazole eluate was diluted with ice-cold buffer (40 mM HEPES, pH 7.4, 5% glycerol) to drop the concentration of KCl to 50 mM. After 20 min incubation on ice, protein droplets were pelleted by centrifugation (10,000g, 10 min, 0°C), washed with 2 column volumes of ice-cold low-salt buffer (40 mM HEPES, pH 7.4, 50 mM KCl, 5% glycerol), and pelleted again. The pellet was resuspended in 5 mL of high-salt buffer (40 mM HEPES, pH 7.4, 500 mM KCl, 5% glycerol), to dissolve protein droplets for the remaining purification steps, and incubated with His_6-Ulp1 protease (2 h). The mixture was incubated with Ni-NTA resin (2 mL, 1 h). Spin-concentrated, flow-through protein was further purified by size exclusion chromatography using the Superdex 75 16/60 column in high-salt buffer at 4°C. Pooled, spin-concentrated, LEM2-containing fractions were dialyzed overnight into storage buffer (40 mM HEPES, pH 7.4, 350 mM KCl, 5% glycerol), spin-concentrated, and aliquoted.

Concentrated protein aliquots were snap-frozen in liquid nitrogen and stored at -80°C for future experiments. Aliquots were thawed and used only once. Final protein concentrations were 260 µM $LEM2_{1-72}$, ~110 µM $LEM2_{NTD}$, 30 µM $LEM2_{NTD\text{-}LINKER\text{-}WH}$, 14 µM $LEM2_{WH}$ and 190 µM His_6-SUMO-$LEM2_{WH}$, 100 µM $LEM2_{Cluster1}$, and 110 µM $LEM2_{Cluster2}$. Note that concentrations of $LEM2_{WH}$ without the tag were limited, and $LEM2_{WH}$ was more stable with the His_6-SUMO tag.

Human, full length LEM2 ($LEM2_{FL}$) was purified as follows. Harvested cells (6-liters expression culture) were resuspended in lysis buffer (5mL per gram cell pellet) containing 25mM HEPES, pH 7.4, 500mM KCl, 1mM DTT, 5% glycerol, lysozyme, 2µg/mL DNase1, and protease inhibitors. Cells were lysed by sonication on ice and clarified (10,000g, 30 min, 4°C). Membranes were pelleted and collected from clarified lysate by ultracentrifugation (100,000g, 1 hr, 4°C). $LEM2_{FL}$ was extracted from membranes with 1% (w/v) n-dodecyl-B-D-maltopyranoside (DDM, Anatrace D310) with stirring (1 hr, 4°C), and collected in the supernatant following centrifugation (35,000g, 30 min, 4°C). DDM-extracted supernatant was supplemented with 10mM imidazole and incubated with Ni-NTA agarose resin (Qiagen) (4 mL bed volume, 1 hr, 4 °C), washed extensively with lysis buffer containing 0.1% DDM, and protein was eluted with 5 column volumes of lysis buffer containing 0.1% DDM and

supplemented with 500mM imidazole, pH 8.0. $LEM2_{FL}$-rich elution fractions were pooled and dialyzed overnight at 4 °C to remove imidazole. The His_6-SUMO tag was cleaved by incubation with His_6-Ulp1 protease (30 min, room temp) and removed by reverse Ni-NTA chromatography. Cleaved, DDM-solubilized $LEM2_{FL}$ was used unconcentrated, or spin-column concentrated (Vivaspin20, 100kDa MWCO, PES) without freeze-thaw.

Purification of CHMP7 proteins: Purification procedures for full-length, human CHMP7 (Uniprot ID Q8WUX9) and point mutants $CHMP7_{R270E+I312E}$, $CHMP7_{R270E+V339D}$, and $CHMP7_{I312E+V339D}$ were adapted from previously published purifications[17]. The truncated $CHMP7_{ESCRT\text{-}III(229\text{-}453)}$ was purified differently. Harvested cells were resuspended in 5 mL ice-cold lysis buffer (40 mM HEPES, pH 8.0, 800 mM KCl, 5% glycerol, 10 mM imidazole, 2 µg/mL DNase1, 5 mM BME, protease inhibitors, and lysozyme) per gram cell pellet. Cells were lysed by sonication, on ice, and clarified (10,000g, 30 min, room temperature). Clarified $CHMP7_{ESCRT\text{-}III}$ lysate was incubated with Ni-NTA agarose resin and spontaneously formed a gel composed of protein polymerized into rings, assayed by negative stain EM. His_6-SUMO-$CHMP7_{ESCRT\text{-}III}$ rings were eluted with imidazole (350 mM), and the eluate was collected with low-speed spin (1,000g) as a gel phase on top of the resin. The gel was scooped off, washed three times with buffer (40 mM HEPES, pH 8.0, 800 mM KCl, 5% glycerol, 1 mM DTT), and polymers were collected by centrifugation (5,000g) each time. The His_6-SUMO tag was cleaved by incubation with His_6-Ulp1 protease (2 h, 4°C). Cleaved $CHMP7_{ESCRT\text{-}III}$ was washed three times with buffer, collected by centrifugation each time, and soluble His_6-SUMO and His_6-Ulp1 were discarded in the aqueous supernatant. Cleaved eluate was diluted with buffer to give a final protein concentration of ~60 µM.

Analytical Size Exclusion Chromatography

$LEM2_{1\text{-}72}$ binding to BAF or BAF-dsDNA complex was assayed by gel filtration chromatography. DNA duplex was prepared as previously described[62]. Combinations of purified $LEM2_{1\text{-}72}$, BAF dimers, and DNA duplexes were combined in 1:1:2 molar ratio. Following incubation at room temperature for 30 min, 50 µL of reaction mixtures were applied to a Superose 6 3.2/300 column (GE Life Sciences) in buffer (20 mM HEPES, pH 7.5, 150 mM NaCl, 5 mM DTT, and 10% glycerol) equilibrated at 4°C. The

flow rate was 40 µL/min for all experiments. Retention volumes for major peaks absorbing at 280 nm (A280) were recorded. The protein contents of peak fractions were assayed by SDS-PAGE.

LEM2 Low Complexity Domain Peptides

Chemically synthesized peptides bearing an N-terminal FITC-Ahx modification (Extended Data Fig. 3A) were purchased from GenScript (Piscataway, NJ), Peptide stock solutions were prepared in milli-Q H2O except $LEM2_{75\text{-}122}$ stocks, which were prepared in DMSO. Phase separation of $LEM2_{75\text{-}122}$ was induced by dilution in milli-Q H2O or buffer (25 mM HEPES, pH 7.4, 150 mM KCl) to 0.2 mg/mL stock.

Turbidimetry

Microtubule bundling by LEM2 was quantified by turbidity (absorbance at 340 nm) (Tecan Spark 10M spectrophotometer)[64]. Reactions (10 µL total volume) of purified $LEM2_{(1\text{-}72,\ NTD,\ WH,\ Cluster1,\ or\ Cluster2)}$ protein or chemically synthesized LEM2 peptides, 1 µM αβ-Tubulin heterodimers polymerized into MTs, KCl (75 mM for LEM2 protein reactions, 0.9 mM for LEM2 peptide reactions), 25 mM HEPES, pH 7.4, 0.5 mM $MgCl_2$, 10 µM paclitaxel (Sigma Aldrich), were prepared at room temperature in 384-well non-binding plates (Grenier Bio-One, #781906). Turbidity was measured, with shaking before each read, for reactions in quadruplicate, and averaged for each condition. Turbidity values for reactions of LEM2 protein/peptide with microtubules were corrected for the turbidity of LEM2 protein/peptide alone, normalized to turbidity of microtubules alone, and plotted (Turbidity a.u.) against [LEM2]. Sigmoidal curve fitting and half-maximum LEM2 concentrations were calculated with GraphPad Prism software. Error bars are standard error of the mean. Turbidity data was corroborated by complementary negative stain electron microscopy. Turbidimetry was not performed for peptides $LEM2_{75\text{-}122}$ or $LEM2_{145\text{-}165}$ with MTs, as these peptides were turbid in the absence of MTs.

Protein labeling for fluorescence imaging

Proteins were fluorescently labeled for microscopy using Microscale Protein Labeling kits from Thermo Scientific: Alexa Fluor™ 488 (A30006), Alexa Fluor™ 555 (A30007) and Alexa Fluor™ 647 (A30009). For imaging experiments, unlabeled protein was supplemented with a minimal amount of

fluorescently labeled protein. $LEM2_{NTD}$ contains a single lysine residue and could not be efficiently labeled with primary amine reactive probes. Instead, His_6-SUMO-$LEM2_{NTD}$ was labeled with Alexa-488™ for fluorescence microscopy and a minimal amount was used to supplement indicated concentrations of unlabeled $LEM2_{NTD}$ for imaging.

Fluorescence microscopy phase separation, coacervation and microtubule bundling assays

Fluorescently labeled proteins were assayed for phase separation, coacervation and MT-bundling with spinning disk confocal microscopy, performed in glass-bottom 384-well plates (Greiner Bio-One # 7781892). Reactions for confocal microscopy were prepared in tubes and transferred to plates for imaging. $LEM2_{NTD}$, $LEM2_{Cluster1}$, $LEM2_{Cluster2}$, and $LEM2_{75\text{-}122}$ droplets were allowed to settle for 15 min before imaging. $LEM2_{NTD}$ droplet formation was induced at room temperature by reducing the salt concentration to 150 mM KCl, keeping the concentrations of other buffer components the same; droplets were allowed to grow 60 minutes before imaging. $LEM2_{NTD}$ droplet (8 to 24 μM) or detergent-solubilized $LEM2_{FL}$ (8 μM) binding to MTs was tested with the addition of fluorescently labeled MTs (1 μM αβ-Tubulin polymerized into MT). MTs were prepared following the Cytoskeleton, Inc. protocol, in a molar ratio of 1:7 HiLyte647-Tubulin:unlabeled Tubulin, in G-PEM buffer (Cytoskeleton Inc. BST01). Unpolymerized tubulin, 1:7 labeled:unlabeled molar ratio, and Alexa555-labeled $LEM2_{WH}$ were tested for association with $LEM2_{NTD}$ droplets at concentrations of 8 μM each. Note that 150 mM KCl promotes MT depolymerization in the absence of stabilizing proteins. To assay coacervate formation, $LEM2_{NTD}$ (8 μM) was fluorescently imaged directly after reducing the salt concentration for $LEM2_{NTD}$ alone or in presence of 1 μM unpolymerized αβ-Tubulin, 30 bases RNA (5'-GGGCCUCCGCCCCCAGUGAGGGGCCGGCCC-3'), or 50 bases DNA (5'-AATGTATTGGTGGGGGCCTGCTCGGGATTGCGGATACGCCCTTGGATTGC-3').

Spinning Disk Confocal Microscopy with Fluorescence Recovery After Photobleaching (FRAP)

To assay $LEM2_{NTD}$ droplet dynamics in FRAP and droplet fusion experiments, 384-well glass-bottom plates were PEGylated using PEG-Silane (LAYSAN BIO, MPEG-SIL-5000) followed by passivation with BSA, according to published protocols to prevent droplet association to silica surface[65].

Spinning disk confocal microscopy with FRAP was carried out using a W1-CSU with a Borealis upgrade (Andor) and ILE Laser Launch (laser lines 405nm, 488nm, 561nm, 647nm; Andor) on a Nikon Eclipse Ti microscope (Nikon Instruments, Inc.) equipped with a Rapp Optoelectronic UGA-40 (Rapp OptoElectronic) photobleaching unit and operated with MicroManager 2.0beta (Open Imaging). Fluorescence images were collected with an Andor Zyla 4.2 cMOS Camera (Oxford Instruments). Samples were imaged using a CFI Plan Apochromat VC 100X Oil NA 1.4 objective (Nikon Instruments, Inc.). Excitation wavelengths were: 488 nm for Alex488TM or FITC; 561 nm for Alex555TM; 640 nm for Alex-647. Photobleaching for FRAP experiments was done with a 473 nm laser (Vortran) for 200 ms per bleach event. Images were recorded with a frequency of 1 Hz, starting with at least one image recorded pre-bleach, including the bleach event, and up to 240 s post-bleaching. Partial and whole droplet FRAP experiments were performed in triplicate, n=17 ($LEM2_{NTD}$), and n=8 ($LEM2_{FL}$) for the bundled-MT FRAP experiment. The ratio of the intensity within bleached regions of interest to background were calculated with ImageJ for each time point and normalized to the intensity at the time of bleaching. Replicates are aligned to the time of bleaching, averaged, and plotted ± standard deviation.

Negative stain electron microscopy

Continuous carbon grids (200-400 mesh copper, Quantifoil) were glow-discharged (PELCO EasiGlow, 15 mA, 0.39 mBar, 30 s). Samples (3 – 5 µL) were stained with 0.75% uranyl formate as described previously[40]. Images were collected with a Tecnai T12 microscope (FEI Company, Hillsboro, USA) with a LaB6 filament, operated at 120 kV, and data was captured with a Gatan Ultrascan CCD camera (Gatan, Inc., Pleasanton, USA). For MT-binding assays, reactions were prepared on grids and incubated for 2 min. MTs were used at a concentration of 1 µM αβ-Tubulin in pre-formed MTs. LEM2 constructs were imaged with MTs (Fig. 2F), at the following concentrations: 6 µM $LEM2_{FL}$, 4 µM $LEM2_{NTD}$, 200 µM $LEM2_{145\text{-}165}$, 80 µM $LEM2_{188\text{-}212}$. Reactions of MTs with $LEM2_{NTD}$ or $LEM2_{188\text{-}212}$, to corroborate turbidimetry, were prepared as described above. Phosphomimetic constructs, $LEM2_{Cluster1}$ and $LEM2_{Cluster2}$, were tested for MT-bundling at 8 µM.

LEM2-induced CHMP7 Polymerization

LEM2 and CHMP7 proteins were mixed at concentrations ranging from 4 - 8 μM in a total volume of 50 μL. $LEM2_{WH}$ or $LEM2_{NTD\text{-}Linker\text{-}WH}$ was present in twofold molar excess to CHMP7 proteins, unless otherwise stated. The buffer was adjusted to between 600 and 800 mM KCl. Reactions were dialyzed for 9-12 h into low-salt buffer (30 mM HEPES, pH 8.0, 25 mM KCl, and 1 mM DTT) using Slide-A-Lyzer MINI Dialysis Device, 10K MWCO (Thermo Fisher Scientific). For experiments including MTs, a 3x stock of pre-formed, lyophilized MTs was prepared in buffer (30 mM HEPES, pH 8.0, 800 mM KCl, 1 mM DTT, 60 uM paclitaxel, and 3 mM $MgCl_2$), and dialysis buffer was supplemented with 10 μM paclitaxel and 1 mM $MgCl_2$. After dialysis, polymeric assemblies were concentrated by low speed centrifugation (5,000 g, 5 min) and resuspended in 30 μL buffer for negative stain EM, SDS-PAGE, or cross-linking mass spectrometry analysis. To determine the stoichiometry of the CHMP7-$LEM2_{WH}$ polymer, CHMP7 (4 μM) was titrated with $LEM2_{WH}$ (0, 0.08, 1 and 4 μM), dialyzed, and polymers were collected by low-speed centrifugation. The supernatant was collected such that 10 μL where left behind as the pellet fraction. Quantities of polymerized and unpolymerized CHMP7 at each LEM2 condition were measured by Coomassie-stained SDS-PAGE, in which equal volumes of pellet and supernatant fractions were loaded. Intensities were quantified by ImageJ. The data was normalized to samples containing 0 and equimolar amounts of $LEM2_{WH}$. The experiment was performed in triplicate, the average was calculated, and error bars are standard deviation.

Liposome preparation

Lipid solutions (Avanti Polar Lipids) were resuspended in chloroform, and liposomes were prepared as previously described[40]. Briefly, lipids (2 mg total) were dried in a glass vial to give final ratio (mole %) of 30% egg phosphatidylserine (PS), 30% egg phosphatidylcholine (PC) and 40% phosphatidylethanolamine (PE). Lipid films were dispersed in buffer (40 mM HEPES, pH 8.0, 150 mM KCl) to produce liposomes at a final concentration of 1 mg/mL, and stored at -80ºC.

Microtubule bundling assay of full length LEM2 in presence of model membranes.

A dried lipid film in a glass vial (1 mg total containing final ratio (mole %) 60% egg PC, 24.7 % PE, 10% bovine liver phosphatidylinositol, 5% cholesterol, and 0.3% 18:1 Liss Rhod PE from Avanti Polar Lipids) was dispersed in buffer (40 mM HEPES, pH 8.0, 800 mM KCl, 5% glycerol, 0.1 % DDM) and sonicated at 30°C for 10 min to produce detergent solubilized lipids at a concentration of 1 mg/mL. Equal volumes detergent-solubilized lipids, activated Bio-Beads™ SM-2 Resin (BioRad), and concentrated $LEM2_{FL}$ (1 mg/mL) or $LEM2_{FL}$ buffer were combined and incubated overnight at 4°C. Detergent-depleted reactions were separated from resin and mixed with fluorescently labeled MT and G-PEM buffer (Cytoskeleton Inc. BST01) to a final KCl concentration of 150 mM and 1 uM Tubulin. Reactions were incubated for 1h at RT before imaging.

Membrane-induced CHMP7 polymerization

CHMP7 was dialyzed or diluted to reduce the salt concentration from 800 mM to 150 mM KCl (supplemented with 5% glycerol, 40 mM HEPES, pH 8.0, 1 mM DTT) to give a final protein concentration of 0.1 mg/ml. Liposomes and CHMP7 were mixed 40:1 (w/w) and negative stain EM grids were prepared immediately.

Electron Microscopy data acquisition and 2D classification

Membrane-induced CHMP7 polymers were prepared for negative stain EM and imaged with a Tecnai T20 microscope (FEI) with a LaB6 filament, operated at 200 kV. 227 micrographs were collected with a TemCam-F816 8k x 8k camera (TVIPS) using SerialEM software[66], with a nominal pixel size of 1.57 Å. The defocus was 0.7 -1.7 µm and the total dose was 20 e-/$Å^2$. Particles containing a repeating polymeric unit were picked manually along the polymeric protein chain, yielding 6094 particles. Specifically, particles were picked from polymers detached from membrane, which were in a favorable orientation for subsequent classification. Particles were picked and 2D-classified with RELION software.

Cross-linking Mass spectrometry

Full length CHMP7 (60 µg) was polymerized with equimolar His_6-SUMO-$LEM2_{WH}$, following the described polymerization assay, and crosslinked with 2 mM light crosslinker (H_{12}-BS3, Creative

Molecules) for 30 min at 30°C. His_6-SUMO-$LEM2_{WH}$ was used to achieve a higher protein concentration. Full length, monomeric CHMP7 (60 µg) was crosslinked with 2 mM heavy crosslinker (D_{12}-BS3, Creative Molecules) under the same conditions. Reactions were quenched (10 mM ammonium bicarbonate, 10 min, room temperature), and light and heavy crosslinked reaction mixtures were combined and processed for mass spectrometry as described previously[67,68]. Crosslinked products were enriched by size-exclusion chromatography (Superdex Peptide, GE Healthcare Life Sciences) as described previously[68] and fractions eluting between 0.9 and 1.4 mL were dried, resuspended in 0.1% formic acid for MS analysis. The fractions starting at 0.9 ml and 1.3 ml were combined prior to evaporation to make four total SEC fractions.

LC-MS analysis was performed with a Q-Exactive Plus mass spectrometer (Thermo Scientific) coupled with a nanoelectrospray ion source (Easy-Spray, Thermo) and NanoAcquity UPLC system (Waters). Enriched fractions were separated on a 15 cm x 75 µm ID PepMap C18 column (Thermo) using a 60-minute gradient from 5-28% solvent B (A: 0.1% formic acid in water, B: 0.1% formic acid in acetonitrile). Precursor MS scans were measured in the Orbitrap scanning from 350-1500 m/z (mass resolution: 70,000). The ten most intense triply charged or higher precursors were isolated in the quadrupole (isolation window: 4 m/z), dissociated by HCD (normalized collision energy: 24), and the product ion spectra were measured in the Orbitrap (mass resolution: 17,500). A dynamic exclusion window of 20 sec was applied and the automatic gain control targets were set to 3e6 (precursor scan) and 5e4 (product scan).

Peaklists were generated using Proteome Discoverer 2.2 (Thermo), and crosslinked peptides searched for with Protein Prospector 5.20.23[69]. 85 of the most intense peaks from each product ion spectrum were searched against a database containing His_6-SUMO-$LEM2_{WH}$ along with the sequences of 10 other proteins comprising CHMP subunits and Tubulin, concatenated with 10 randomized decoy versions of each of these sequences (121 sequences total). Search parameters were: mass tolerance of 20 ppm (precursor) and 30 ppm (product); fixed modifications of carbamidomethylation on cysteine; variable modifications of peptide N-terminal glutamine conversion to pyroglutamate, oxidation of

methionine, and "dead-end" modification of lysine and the protein N-terminus by semi-hydrolyzed heavy and light BS3; trypsin specificity was used with 2 missed cleavages and three variable modifications per peptide were allowed. Unique, crosslinked residue pairs were reported at a 1.5% FDR threshold, corresponding to a Score Difference cutoff of 15.

For quantitative analysis, precursor ion filtering in Skyline 4.1[70] was used to extract light:heavy crosslinked precursor ion signals. Skyline does not directly support crosslinking analysis, so crosslinked peptides were linearized and exported as a spectral library as previously described[71]. Transitions were generated for every light or heavy crosslinked peptide species discovered in the Protein Prospector search and paired with its corresponding heavy or light counterpart. Precursor ion transitions matching the first three isotopes were extracted across all four LC-MS fractions. Each extracted ion chromatogram was manually inspected and the start and end points were adjusted to ensure that the correct peaks were detected and that there were no interfering signals. Isotope dot products were required to exceed 0.85. The peak areas were re-imported into R and summarized at the level of crosslinked residues for each light and heavy crosslink. Peak areas were summed for all peptides matching a given crosslink. Finally, log2 ratios of the heavy to light peak areas were determined. Filtered cross-links were mapped to the primary protein structure using xiNET[72].

Homology modeling and cross-link mapping

Homology models of human CHMP7 and LEM2 domains were created with Phyre2[73] (Table 2). Reference structures were selected based on confidence scores and homology to reference structure. Models were validated by mapping cross-linking data to the models using UCSF Chimera[74] together with Xlink analyzer[75].

Immunostaining for fluorescence microscopy

Cells were fixed at room temperature in 2% paraformaldehyde for 25 min. The primary antibodies used for immunodetection were rabbit α-IST1[76], rabbit α-Tubulin (ab18251; abcam), rat α-Tubulin (YL1/2; Accurate Chemical & Scientific), SUN2 (gift from Brian Burke), and mouse α-53BP1 (MAB3802; Millipore). After incubation with fluorescently labeled secondary antibodies (α-rabbit 488,

α-mouse 488, α-rabbit 647, and α-rabbit 568; Thermo Fisher), coverslips were mounted with DAPI ProLong Gold (Thermo Fisher) and imaged by either widefield microscopy (Zeiss Axioskop 2; Axiovision software), spinning disk confocal microscopy (Nikon Eclipse T*i*; Metamorph software), or stimulated emission depletion microscopy (see below). For quantifying IST1 localization: α-rabbit 488 against rabbit α-IST1; for assessing DNA Damage in telophase cells: α-mouse 488 against mouse α-53BP1 and α-rabbit 568 against rabbit α-Tubulin; for quantifying the tubulin and nuclear envelope phenotype in telophase cells: α-mouse 488 against mouse α-SUN2 and α-rabbit 568 against rabbit α-Tubulin; for interphase phenotypes: α-rabbit 488 against rabbit α-Tubulin; for STED: α-mouse 568 against mouse α-Tubulin and α-rabbit 647 against rabbit α-LEM2.

Stimulated Emission Depletion (STED) microscopy

STED microscopy was performed on a Leica TCS SP8 STED 3X confocal laser-scanning microscope equipped with a HC PL APO CS2 100x/1.40 OIL objective. Confocal sections were imaged with Leica LAS X Core software and processed with Huygens Software Suite (SVI). Images were recorded using 405 nm laser line at 1.4% laser power to image DAPI, and a 572 nm Laser line at 5.6% laser power to image Tubulin in confocal detector mode. LEM2 was imaged with a 653 nm laser line at 2.5% laser power in STED pulsed detector mode (gate start at 0.3 ns and gate end at 6.5 ns) with a Huygens saturation factor of 5.7. Deconvolved Images were further processed in ImageJ (NIH).

Statistics

For time-lapse colocalization experiments tracking GFP-CHMP7 with either LEM2-mChr or $LEM2_{\Delta WH}$-mChr, data was collected across three independent experiments and individual points corresponding to each cell (two disks) were plotted showing standard deviation (LEM2-mChr: n=14; $LEM2_{\Delta WH}$-mChr: n=11; see below for method of quantification). For quantification of IST1 recruitment, the mean percent of anaphase disks for each category of IST1 recruitment was determined from three independent experiments and plotted showing standard error of the mean; although robust and extra robust were quantified as separate categories, they are graphed as a single category for clarity (see below

for method of quantification; sample size (*n*) and raw data shown in Table 1). For quantification of nuclear accumulation of NLS-3xGFP in anaphase, data was collected across more than three independent experiments and the mean plotted showing standard deviation (siControl LEM2-mChr: *n*=26; siLEM2-2 LEM2-mChr: *n*=44; siControl LEM2$_{\Delta S\text{-}Y}$-mChr: *n*=18; siLEM2-2 LEM2$_{\Delta S\text{-}Y}$-mChr: *n*=20; siControl LEM2$_{\Delta P\text{-}R}$-mChr: *n*=10; siLEM2-2 LEM2$_{\Delta P\text{-}R}$-mChr: *n*=18; siControl LEM2$_{\Delta WH}$-mChr: *n*=24; siLEM2-2 LEM2$_{\Delta WH}$-mChr: *n*=14; see below for method of quantification). For quantification of nuclear accumulation of NLS-3xGFP 30 minutes following cleavage furrow ingression, data was collected across three independent experiments and the mean plotted showing standard deviation (siControl: *n*=29; siLEM2-2: *n*=50; siCHMP7: *n*=31). For quantification of NE-tubulin defects in telophase cells, the mean percent of telophase cells with NE-tubulin defects was determined from three independent experiments and plotted showing standard error of the mean (siControl: *n*=75, 35, 37; siLEM2-1: *n*=72, 35, 37; siLEM2-2: *n*=45, 34, 34). For quantification of DNA damage in telophase cells, the mean percent of telophase cells with ≥5 53BP1 foci was determined from three independent experiments and plotted showing standard error of the mean (siControl: *n*=56, 52, 44; siLEM2-1: *n*=64, 56, 26; siLEM2-2: *n*=74, 50, 40). For quantification of the circularity of interphase nuclei, the mean percent of cells with circularity values between 0.000-0.199, 0.200-0.399, 0.400-0.599, 0.600-0.799, 0.800-1.000 was determined from three independent experiments and plotted showing standard error of the mean (siControl parental: *n*=105, 46, 80; siLEM2-2 parental: *n*=102, 116, 59; siControl LEM2-mChr: *n*=153, 53, 122; siLEM2-2 LEM2-mChr: *n*=84, 81, 105; siControl LEM2$_{\Delta S\text{-}Y}$-mChr: *n*=123, 68, 144; siLEM2-2 LEM2$_{\Delta S\text{-}Y}$-mChr: *n*=93, 95, 105; siControl LEM2$_{\Delta P\text{-}R}$-mChr: *n*=149, 123, 58; siLEM2-2 LEM2$_{\Delta P\text{-}R}$-mChr: *n*=49, 31, 42; siControl LEM2$_{\Delta WH}$-mChr: *n*=116, 96, 94; siLEM2-2 LEM2$_{\Delta WH}$-mChr: *n*=85, 32, 68; see below for method of quantification).

In all cases, two-tailed unpaired t-test was used to determine p-values, which, unless otherwise specified, are indicated as follows: **P* < 0.05; ***P* < 0.005; N.S., not significant.

Quantification from fluorescence microscopy

For illustration, images of anaphase A and B cells were acquired by widefield microscopy at 100X and adjusted so that background fluorescence in the DNA, IST1, and LEM2-mChr channels were comparable between samples. Raw images acquired by widefield microscopy at 100X were used to score the IST1 phenotype in anaphase A (early) and anaphase B (late). IST1 localization to anaphase chromatin masses was assessed in three independent experiments in which images were randomized and quantified blindly by three independent scorers. Each chromatin disk (two per cell) was scored as having extra robust, robust, weak, or no recruitment for IST1. Robust recruitment was characterized by distinctive foci organized at the core of chromatin masses, whereas weak recruitment was characterized by less intense, often fewer, and less organized foci at the chromatin surface, consistent with what has previously been shown[17]. Extra robust was characterized by strikingly intense IST1 fluorescence, often accompanied by recruitment over most of the chromatin disk. For clarity, the robust and extra robust categories were graphed together as a single category. The majority score was used in cases where the three scores differed.

For time-lapse colocalization experiments tracking GFP-CHMP7, images of anaphase cells were acquired by spinning disk confocal microscopy at 60X and were selected for scoring at the time of peak LEM2-mCherry or $LEM2_{\Delta WH}$-mCherry enrichment at the core region of anaphase chromatin disks. In FIJI, each cell was thresholded for either LEM2-mCherry or $LEM2_{\Delta WH}$-mCherry enrichment. The mean fluorescence (arbitrary units) was measured for each region of interest in the GFP-CHMP7 channel. The regions of interest were subtracted from the area of the whole cell to measure the mean fluorescence of cytoplasmic GFP-CHMP7 for each anaphase cell. The plotted values are the mean GFP-CHMP7 fluorescence of the region of interest, as determined by exogenous LEM2 enrichment, normalized to the mean fluorescence of cytoplasmic GFP-CHMP7. Plotted points are for individual cells, which were imaged across three different experiments.

Nuclear accumulation of NLS-3xGFP in late anaphase was determined by taking the ratio of nuclear to cytoplasmic NLS-3xGFP at one-minute intervals throughout anaphase after imaging at 15 s

intervals by spinning disk confocal microscopy at 60X. In FIJI, regions of chromatin were defined as regions of interest in the NucBlue™ channel and used to measure the mean fluorescence (arbitrary units) in the NLS-3xGFP channel. Cytoplasmic levels of NLS-3xGFP were determined by selecting the whole cell, and subsequently deselecting the regions of chromatin. The mean fluorescence of nuclear NLS-3xGFP for each disk was then divided by the mean fluorescence of cytoplasmic NLS-3xGFP of the same cell. Data was collected across more than three independent experiments and plotted showing standard deviation.

Nuclear accumulation of NLS-3xGFP in telophase was determined by taking the ratio of nuclear to cytoplasmic NLS-3xGFP 30 minutes after complete cleavage furrow ingression. Cells were live imaged by spinning disk confocal microscopy at 60X. In FIJI, regions of chromatin were defined as regions of interest in the NucBlue™ channel and used to measure the integrated density (the product of area and mean gray value) in the NLS-3xGFP channel. Cytoplasmic levels of NLS-3xGFP were determined by selecting the whole cell and subsequently deselecting the regions of chromatin. The integrated density of nuclear NLS-3xGFP for each disk was then divided by the integrated density of cytoplasmic NLS-3xGFP of the same cell. Since compartmentalization was quantified at 30 minutes after complete cleavage furrow ingression, integrated density was used to account for nuclear size. Data was collected across more than three independent experiments and plotted showing standard deviation.

For the purposes of illustration, interphase and telophase cells were acquired by widefield and spinning disk confocal microscopy at 60X and were adjusted so that background fluorescence was comparable between samples. Raw images used to score the nuclear envelope and tubulin phenotype in telophase were acquired by widefield microscopy at 60X in three independent experiments. To score DNA damage in telophase, images from three independent experiments were acquired by widefield microscopy at 60X and thresholded uniformly in FIJI. Nuclear foci were detected using the find maxima function in FIJI and noise tolerance was held constant for all conditions. To score interphase nuclear circularity, images from three independent experiments were acquired by widefield microscopy at 60X. The DNA channel was thresholded in FIJI and each nucleus was defined as a region of interest. The

nuclei were then assessed for their circularity (*circularity = 4pi(area/perimeter^2)*, as described by others[77].

Time-Lapse Light Microscopy Analysis

For all live imaging experiments images were acquired at 60X and complete cleavage furrow ingression is designated as t=0 minutes.

Stable cell lines used in this study are described in Table 4. Cells stably expressing GFP-Lamin B2 and LEM2-mCherry were plated on fibronectin coated Mat-Tek dishes and cultured for 48 hours. Cells were treated 200nM SiR-Tubulin (CY-SC006; Cytoskelton, Inc.) and NucBlue™ (Thermo Fisher) 1 hr prior to live-imaging by spinning disk confocal microscopy.

Cells stably expressing GFP-Tubulin[78] were transiently transfected with siRNA resistant pCMV(Δ5)-LEM2-mCherry (PL13), pCMV(Δ5)-LEM2m21-mCherry (PL14), pCMV(Δ5)-LEM2$_{\Delta LCD}$-mCherry (PL15), pCMV(Δ5)-LEM2$_{\Delta S\text{-}Y}$-mCherry (PL16), pCMV(Δ5)-LEM2$_{\Delta P\text{-}R}$-mCherry (PL17), or pCMV(Δ5)-LEM2$_{\Delta WH}$-mCherry (PL18) using Lipofectamine LTX Plus (Thermo Fisher) for 24 h. Cells were then re-plated on Mat-Tek dishes 8 h before being arrested at G1/S and released, as described below. Twelve hours after release, cells were live-imaged by spinning disk confocal microscopy in the presence of NucBlue™ (Thermo Fisher).

For time-lapse colocalization experiments, HeLa cells stably expressing GFP-CHMP7 were transiently transfected with either siRNA resistant pCMV(Δ5)-LEM2-mCherry (PL13) or siRNA resistant pCMV(Δ5)-LEM2$_{\Delta WH}$-mCherry (PL17) using Lipofectamine LTX Plus (Thermo Fisher) for 24 h. Cells were then re-plated on Mat-Tek dishes 8 h before being arrested at G1/S and released, as described below. Twelve hours after release, cells were live-imaged by spinning disk confocal microscopy.

To track nuclear integrity, cells stably expressing NLS-3xGFP (PL19) alone or combined with either siRNA resistant LEM2-mCherry (PL13), LEM2$_{\Delta S\text{-}Y}$-mChr (PL16), LEM2$_{\Delta P\text{-}R}$-mChr (PL17), or LEM2$_{\Delta WH}$-mCherry (PL18) were plated on Mat-Tek dishes in the presence of siRNA 8 h before being arrested at G1/S and released, as described below. Twelve hours after release, cells were live-imaged by spinning disk confocal microscopy in the presence of NucBlue™ (Thermo Fisher) in either 15-second

intervals throughout anaphase or 3-minute intervals following complete cleavage furrow ingression throughout telophase. In the latter experiments, 100 nM SiR-Tubulin (CY-SC006; Cytoskelton, Inc.) was added 1 hr prior to imaging.

For siRNA depletion in HeLa cells stably expressing H2B-mCherry and GFP-Tubulin, cells were plated on fibronectin coated Mat-Tek dishes in the presence of siRNA 8 h before being arrested at G1/S and released, as described below. Twelve hours after release, cells were live-imaged by spinning disk confocal microscopy.

Cells stably expressing GFP-BAF and LEM2-mCherry were plated on fibronectin coated Mat-Tek dishes 8 h before being arrested at G1/S and released, as described below. Twelve hours after release, cells were live-imaged by spinning disk confocal microscopy.

siRNA-Mediated Depletion and Cell-Cycle Synchronization

HeLa and U2OS cells were plated on fibronectin-coated coverslips in the presence of 10 nM siRNA oligo, delivered by Lipofectamine RNAiMAX Transfection Reagent (Thermo Fisher). Specific sequences used were: siControl [siScr-1[78,79]], siLEM2-1 [antisense sequence targeting nucleotides 78–98: UUGCGGUAGACAUCCCGGGdTdT[34]], and siLEM2-2 [antisense sequence targeting nucleotides 1,297–1,317: UACAUAUGGAUAGCGCUCCdTdT[34]]. In experiments testing whether exogenous LEM2 could rescue function after endogenous LEM2 depletion, siLEM2-2 was used to deplete endogenous LEM2 as exogenous LEM2 constructs harbor silent mutations that confer resistance to the siLEM2-2 oligo. Culture medium containing 2 mM thymidine was then added for 24 h to arrest cells at G1/S. Cells were then rinsed thoroughly with PBS, followed by the addition of culture media. Twelve hours after release, cells were imaged live or fixed for microscopy. For experiments tracking interphase phenotypes, cells were fixed for immunostaining sixteen hours after release.

For assessing the phosphorylation status of exogenous LEM2 at different stages of the cell cycle, cells were arrested at G1/S by treating with culture medium containing 2 mM thymidine for 24 h. G1/S-arrested cells were then either harvested or thoroughly rinsed with PBS before the addition of culture media containing 100ng/mL nocodazole. After 16 h of nocodazole treatment, mitotic cells were harvested

by shake off. Cell pellets were rinsed in TBS before lysis and separation by Phos-Tag™ acrylamide SDS-PAGE and subsequent immunoblot (described below).

Immunoblots

To verify efficacy of siRNA treatments and expression of siRNA-resistant constructs, cells were plated in six-well dishes and subjected to the same experimental conditions as those used to generate imaging data. Whole cell lysates were prepared with NP40 lysis buffer and volume adjusted to normalize total protein concentration before being diluted in SDS sample buffer supplemented with β-mercaptoethanol for boiling. Samples were run on 10% SDS-PAGE gels and wet transferred to PVDF membrane. 3% milk in TBS-T was used for blocking and antibody dilutions. After incubation with primary antibodies [α-LEM2 (HPA017340; Sigma-Aldrich) or α-Tubulin (ab18251; abcam)], reactivity was detected with HRP-coupled secondary antibodies (Thermo Fisher) and chemiluminescence.

To assess phosphorylation of exogenous LEM2 by mobility shift, whole cell lysates were prepared and volume adjusted to equalize total protein concentration using NP40 lysis buffer lacking EDTA and phosphatase inhibitors. Aliquots of each lysate were then subjected to either lambda protein phosphatase treatment per the manufacturer's instructions (P0753S; NEB) or a control reaction containing only PMP buffer and $MnCl_2$. Samples were then diluted in SDS sample buffer supplemented with β-mercaptoethanol and boiled. Samples were run on a 10% SDS-PAGE gel prepared with Phos-Tag™ Acrylamide reagent (AAL-107; Waco) per the manufacturer's instructions. The gel was incubated in transfer buffer with 10mM EDTA before wet transfer to PVDF membrane. Detection of LEM2 by immunoblot was performed as described above.

References

1. Cuylen, S. *et al.* Ki-67 acts as a biological surfactant to disperse mitotic chromosomes. *Nature* (2016). doi:10.1038/nature18610
2. Ungricht, R. & Kutay, U. Mechanisms and functions of nuclear envelope remodelling. *Nature Reviews Molecular Cell Biology* **18**, 229–245 (2017).
3. Mehsen, H. *et al.* PP2A-B55 promotes nuclear envelope reformation after mitosis in Drosophila. *J. Cell Biol.* **217**, 4106–4123 (2018).
4. Cundell, M. J. *et al.* A PP2A-B55 recognition signal controls substrate dephosphorylation kinetics during mitotic exit. *J. Cell Biol.* (2016). doi:10.1083/jcb.201606033
5. Kim, H.-S., Fernandes, G. & Lee, C.-W. Protein Phosphatases Involved in Regulating Mitosis: Facts and Hypotheses. *Mol. Cells* **39**, 654–662 (2016).
6. Asencio, C. *et al.* Coordination of kinase and phosphatase activities by Lem4 enables nuclear envelope reassembly during mitosis. *Cell* (2012). doi:10.1016/j.cell.2012.04.043
7. Samwer, M. *et al.* DNA Cross-Bridging Shapes a Single Nucleus from a Set of Mitotic Chromosomes. *Cell* (2017). doi:10.1016/j.cell.2017.07.038
8. Otsuka, S. *et al.* Postmitotic nuclear pore assembly proceeds by radial dilation of small membrane openings. *Nat. Struct. Mol. Biol.* (2017). doi:10.1038/s41594-017-0001-9
9. Vietri, M. *et al.* Spastin and ESCRT-III coordinate mitotic spindle disassembly and nuclear envelope sealing. *Nature* **522**, 231–235 (2015).
10. LaJoie, D. & Ullman, K. S. Coordinated events of nuclear assembly. *Current Opinion in Cell Biology* **46**, (2017).
11. Haraguchi, T. *et al.* Live cell imaging and electron microscopy reveal dynamic processes of BAF-directed nuclear envelope assembly. *J. Cell Sci.* (2008). doi:10.1242/jcs.033597
12. Liu, S. *et al.* Nuclear envelope assembly defects link mitotic errors to chromothripsis. *Nature* (2018). doi:10.1038/s41586-018-0534-z

13. Berk, J. M., Tifft, K. E. & Wilson, K. L. The nuclear envelope LEM-domain protein emerin. *Nucleus (United States)* (2013). doi:10.4161/nucl.25751

14. Tapia, O., Fong, L. G., Huber, M. D., Young, S. G. & Gerace, L. Nuclear envelope protein Lem2 is required for mouse development and regulates MAP and AKT kinases. *PLoS One* (2015). doi:10.1371/journal.pone.0116196

15. Brachner, A. LEM2 is a novel MAN1-related inner nuclear membrane protein associated with A-type lamins. *J. Cell Sci.* (2005). doi:10.1242/jcs.02701

16. Yam, C., He, Y., Zhang, D., Chiam, K. H. & Oliferenko, S. Divergent strategies for controlling the nuclear membrane satisfy geometric constraints during nuclear division. *Curr. Biol.* (2011). doi:10.1016/j.cub.2011.06.052

17. Gu, M. *et al.* LEM2 recruits CHMP7 for ESCRT-mediated nuclear envelope closure in fission yeast and human cells. *Proc. Natl. Acad. Sci.* **114**, E2166–E2175 (2017).

18. Thaller, D. J. *et al.* An ESCRT-LEM protein surveillance system is poised to directly monitor the nuclear envelope and nuclear transport system. *Elife* (2019). doi:10.7554/eLife.45284

19. Webster, B. M. *et al.* Chm7 and Heh1 collaborate to link nuclear pore complex quality control with nuclear envelope sealing. *EMBO J.* (2016). doi:10.15252/embj.201694574

20. Olmos, Y., Hodgson, L., Mantell, J., Verkade, P. & Carlton, J. G. ESCRT-III controls nuclear envelope reformation. *Nature* **522**, 236–239 (2015).

21. Schöneberg, J. *et al.* ATP-dependent force generation and membrane scission by ESCRT-III and Vps4. *Science* (2018). doi:10.1126/science.aat1839

22. Yam, C., Gu, Y. & Oliferenko, S. Partitioning and remodeling of the Schizosaccharomyces japonicus mitotic nucleus require chromosome tethers. *Curr. Biol.* (2013). doi:10.1016/j.cub.2013.09.057

23. Pfitzner, A.-K., Mercier, V. & Roux, A. Vps4 triggers sequential subunit exchange in ESCRT-III polymers that drives membrane constriction and fission. *bioRxiv* (2019). doi:10.1101/718080

24. Ventimiglia, L. N. *et al.* CC2D1B Coordinates ESCRT-III Activity during the Mitotic

Reformation of the Nuclear Envelope. *Developmental Cell* (2018). doi:10.1016/j.devcel.2018.11.012

25. Vietri, M. *et al.* Unrestrained ESCRT-III drives chromosome fragmentation and micronuclear catastrophe. *bioRxiv* 517011 (2019). doi:10.1101/517011

26. Willan, J. *et al.* ESCRT-III is necessary for the integrity of the nuclear envelope in micronuclei but is aberrant at ruptured micronuclear envelopes generating damage. *Oncogenesis* (2019). doi:10.1038/s41389-019-0136-0

27. Olmos, Y., Perdrix-Rosell, A. & Carlton, J. G. Membrane Binding by CHMP7 Coordinates ESCRT- III-Dependent Nuclear Envelope Reformation. *Curr. Biol.* (2016). doi:10.1016/j.cub.2016.07.039

28. McCullough, J., Frost, A. & Sundquist, W. I. Structures, Functions, and Dynamics of ESCRT-III/Vps4 Membrane Remodeling and Fission Complexes. *Annu. Rev. Cell Dev. Biol.* (2018). doi:10.1146/annurev-cellbio-100616-060600

29. Im, Y. J. & Hurley, J. H. Integrated Structural Model and Membrane Targeting Mechanism of the Human ESCRT-II Complex. *Dev. Cell* (2008). doi:10.1016/j.devcel.2008.04.004

30. Im, Y. J., Wollert, T., Boura, E. & Hurley, J. H. Structure and Function of the ESCRT-II-III Interface in Multivesicular Body Biogenesis. *Dev. Cell* (2009). doi:10.1016/j.devcel.2009.07.008

31. Banani, S. F., Lee, H. O., Hyman, A. A. & Rosen, M. K. Biomolecular condensates: Organizers of cellular biochemistry. *Nature Reviews Molecular Cell Biology* (2017). doi:10.1038/nrm.2017.7

32. Alberti, S., Gladfelter, A. & Mittag, T. Considerations and Challenges in Studying Liquid-Liquid Phase Separation and Biomolecular Condensates. *Cell* (2019). doi:10.1016/j.cell.2018.12.035

33. Shin, Y. & Brangwynne, C. P. Liquid phase condensation in cell physiology and disease. *Science* (2017). doi:10.1126/science.aaf4382

34. Ulbert, S., Antonin, W., Platani, M. & Mattaj, I. W. The inner nuclear membrane protein Lem2 is critical for normal nuclear envelope morphology. *FEBS Lett.* (2006). doi:10.1016/j.febslet.2006.10.060

35. Lee, K. K. *et al.* Distinct functional domains in emerin bind lamin A and DNA-bridging protein BAF. *J Cell Sci* (2001). doi:http://dx.doi.org/10.1016/B978-0-08-091812-9.50011-9

36. Haraguchi, T. *et al.* BAF is required for emerin assembly into the reforming nuclear envelope. *J. Cell Sci.* (2001).

37. Boeynaems, S. *et al.* Spontaneous driving forces give rise to protein−RNA condensates with coexisting phases and complex material properties. *Proc. Natl. Acad. Sci.* (2019). doi:10.1073/pnas.1821038116

38. Hughes, M. P. *et al.* Atomic structures of low-complexity protein segments reveal kinked b sheets that assemble networks. *Science* (2018). doi:10.1126/science.aan6398

39. Caputo, S. *et al.* The carboxyl-terminal nucleoplasmic region of MAN1 exhibits a DNA binding winged helix domain. *J. Biol. Chem.* (2006). doi:10.1074/jbc.M601980200

40. McCullough, J. *et al.* Structure and membrane remodeling activity of ESCRT-III helical polymers. *Science* (2015). *doi: 10.1126/science.aad8305*

41. Tang, S. *et al.* Structural basis for activation, assembly and membrane binding of ESCRT-III Snf7 filaments. *Elife* (2015). doi:10.7554/eLife.12548

42. Hornbeck, P. V. *et al.* PhosphoSitePlus, 2014: Mutations, PTMs and recalibrations. *Nucleic Acids Res.* (2015). doi:10.1093/nar/gku1267

43. Kinoshita, E., Kinoshita-Kikuta, E., Takiyama, K. & Koike, T. Phosphate-binding tag, a new tool to visualize phosphorylated proteins. *Mol. Cell. Proteomics* (2006). doi:10.1074/mcp.T500024-MCP200

44. Hernández-Vega, A. *et al.* Local Nucleation of Microtubule Bundles through Tubulin Concentration into a Condensed Tau Phase. *Cell Rep.* (2017). doi:10.1016/j.celrep.2017.08.042

45. Yu, C.-H. *et al.* Central-spindle microtubules are strongly coupled to chromosomes during both anaphase A and anaphase B. *Mol. Biol. Cell* **30**, 2503–2514 (2019).

46. Wang, J. *et al.* A Molecular Grammar Governing the Driving Forces for Phase Separation of Prion-like RNA Binding Proteins. *Cell* (2018). doi:10.1016/j.cell.2018.06.006

47. Gallivan, J. P. & Dougherty, D. A. Cation-pi interactions in structural biology. *Proc. Natl. Acad. Sci.* (1999). doi:10.1073/pnas.96.17.9459

48. Marbach, F. *et al.* The Discovery of a LEMD2-Associated Nuclear Envelopathy with Early Progeroid Appearance Suggests Advanced Applications for AI-Driven Facial Phenotyping. *Am. J. Hum. Genet.* (2019). doi:10.1016/j.ajhg.2019.02.021

49. Boone, P. M. *et al.* Hutterite-type cataract maps to chromosome 6p21.32-p21.31, cosegregates with a homozygous mutation in LEMD2, and is associated with sudden cardiac death. *Mol. Genet. Genomic Med.* (2016). doi:10.1002/mgg3.181

50. Denais, C. M. *et al.* Nuclear envelope rupture and repair during cancer cell migration. *Science* (2016). doi:10.1126/science.aad7297

51. Halfmann, C. T. *et al.* Repair of nuclear ruptures requires barrier-to-autointegration factor. *J. Cell Biol.* (2019). doi:10.1083/jcb.201901116

52. Raab, M. *et al.* ESCRT III repairs nuclear envelope ruptures during cell migration to limit DNA damage and cell death. *Science* (2016). doi:10.1126/science.aad7611

53. Larson, A. G. *et al.* Liquid droplet formation by HP1α suggests a role for phase separation in heterochromatin. *Nature* (2017). doi:10.1038/nature22822

54. Barrales, R. R., Forn, M., Georgescu, P. R., Sarkadi, Z. & Braun, S. Control of heterochromatin localization and silencing by the nuclear membrane protein Lem2. *Genes Dev.* (2016). doi:10.1101/gad.271288.115

55. Penfield, L. *et al.* Dynein-pulling forces counteract lamin-mediated nuclear stability during nuclear envelope repair. *Mol. Biol. Cell* (2018). doi:10.1091/mbc.E17-06-0374

56. Barton, L. J., Soshnev, A. A. & Geyer, P. K. Networking in the nucleus: A spotlight on LEM-domain proteins. *Current Opinion in Cell Biology* (2015). doi:10.1016/j.ceb.2015.03.005

57. Beutel, O., Maraspini, R., Pombo-Garcia, K., Martin-Lemaitre, C. & Honigmann, A. Phase Separation of Zonula Occludens Proteins Drives Formation of Tight Junctions. *SSRN Electron. J.* (2019). doi:10.2139/ssrn.3362257

58. Milovanovic, D., Wu, Y., Bian, X. & De Camilli, P. A liquid phase of synapsin and lipid vesicles. *Science* (2018). doi:10.1126/science.aat5671

59. Dimova, R. & Lipowsky, R. Lipid membranes in contact with aqueous phases of polymer solutions. *Soft Matter* (2012). doi:10.1039/c2sm25261a

60. Lipowsky, R. Bending of membranes by anchored polymers. *EPL* (1995). doi:10.1209/0295-5075/30/4/002

61. Zeno, W. F. *et al.* Synergy between intrinsically disordered domains and structured proteins amplifies membrane curvature sensing. *Nat. Commun.* (2018). doi:10.1038/s41467-018-06532-3

62. Bradley, C. M., Ronning, D. R., Ghirlando, R., Craigie, R. & Dyda, F. Structural basis for DNA bridging by barrier-to-autointegration factor. *Nat. Struct. Mol. Biol.* (2005). doi:10.1038/nsmb989

63. Cai, M. *et al.* Solution NMR structure of the barrier-to-autointegration factor-emerin complex. *J. Biol. Chem.* (2007). doi:10.1074/jbc.M700576200

64. Hamon, L., Savarin, P., Curmi, P. A. & Pastré, D. Rapid assembly and collective behavior of microtubule bundles in the presence of polyamines. *Biophys. J.* (2011). doi:10.1016/j.bpj.2011.05.022

65. Gibson, B. A. *et al.* Organization of Chromatin by Intrinsic and Regulated Phase Separation. *Cell* (2019). doi:10.1016/j.cell.2019.08.037

66. Mastronarde, D. N. Automated electron microscope tomography using robust prediction of specimen movements. *J. Struct. Biol.* (2005). doi:10.1016/j.jsb.2005.07.007

67. Bui, K. H. *et al.* Integrated structural analysis of the human nuclear pore complex scaffold. *Cell* **155**, 1233–1243 (2013).

68. Leitner, A. *et al.* Expanding the Chemical Cross-Linking Toolbox by the Use of Multiple Proteases and Enrichment by Size Exclusion Chromatography. *Mol. Cell. Proteomics* (2012). doi:10.1074/mcp.M111.014126

69. Trnka, M. J., Baker, P. R., Robinson, P. J. J., Burlingame, A. L. & Chalkley, R. J. Matching Cross-linked Peptide Spectra: Only as Good as the Worse Identification. *Mol. Cell. Proteomics*

(2014). doi:10.1074/mcp.M113.034009

70. Schilling, B. *et al.* Platform-independent and Label-free Quantitation of Proteomic Data Using MS1 Extracted Ion Chromatograms in Skyline. *Mol. Cell. Proteomics* (2012). doi:10.1074/mcp.M112.017707

71. Muller, F., Fischer, L., Chen, Z. A., Auchynnikava, T. & Rappsilber, J. On the Reproducibility of Label-Free Quantitative Cross-Linking/Mass Spectrometry. *J. Am. Soc. Mass Spectrom.* **29**, 405–412 (2018).

72. Combe, C. W., Fischer, L. & Rappsilber, J. xiNET: Cross-link Network Maps With Residue Resolution. *Mol. Cell. Proteomics* (2015). doi:10.1074/mcp.O114.042259

73. Kelley, L. A., Mezulis, S., Yates, C. M., Wass, M. N. & Sternberg, M. J. E. The Phyre2 web portal for protein modeling, prediction and analysis. *Nat. Protoc.* **10**, 845 (2015).

74. Pettersen, E. F. *et al.* UCSF Chimera - A visualization system for exploratory research and analysis. *J. Comput. Chem.* (2004). doi:10.1002/jcc.20084

75. Kosinski, J. *et al.* Xlink analyzer: Software for analysis and visualization of cross-linking data in the context of three-dimensional structures. *J. Struct. Biol.* **189**, 177–183 (2015).

76. Bajorek, M. *et al.* Biochemical Analyses of Human IST1 and Its Function in Cytokinesis. *Mol. Biol. Cell* (2009). doi:10.1091/mbc.E08-05-0475

77. Donahue, D. A. *et al.* SUN2 Overexpression Deforms Nuclear Shape and Inhibits HIV. *J. Virol.* (2016). doi:10.1128/jvi.03202-15

78. Mackay, D. R., Makise, M. & Ullman, K. S. Defects in nuclear pore assembly lead to activation of an Aurora B-mediated abscission checkpoint. *J. Cell Biol.* (2010). doi:10.1083/jcb.201007124

79. Mackay, D. R., Elgort, S. W. & Ullman, K. S. The Nucleoporin Nup153 Has Separable Roles in Both Early Mitotic Progression and the Resolution of Mitosis. *Mol. Biol. Cell* (2009). doi:10.1091/mbc.e08-08-0883

80. Muzioł, T. *et al.* Structural Basis for Budding by the ESCRT-III Factor CHMP3. *Dev. Cell* (2006). doi:10.1016/j.devcel.2006.03.013

Publishing Agreement

It is the policy of the University to encourage open access and broad distribution of all theses, dissertations, and manuscripts. The Graduate Division will facilitate the distribution of UCSF theses, dissertations, and manuscripts to the UCSF Library for open access and distribution. UCSF will make such theses, dissertations, and manuscripts accessible to the public and will take reasonable steps to preserve these works in perpetuity.

I hereby grant the non-exclusive, perpetual right to The Regents of the University of California to reproduce, publicly display, distribute, preserve, and publish copies of my thesis, dissertation, or manuscript in any form or media, now existing or later derived, including access online for teaching, research, and public service purposes.

DocuSigned by:
Isabel Emily Johnson
E299543138A140B...
Author Signature

2/26/2020
Date